Potential of the Synthetic Fuel Oxymethylene Ether (OME) for the Usage in a Single-Cylinder Non-Road Diesel Engine: Thermodynamics and Emissions

Florian Zacherl [1,*], Christoph Wopper [1], Peter Schwanzer [2] and Hans-Peter Rabl [1]

1   Ostbayerische Technische Hochschule (OTH) Regensburg, Laboratory of Combustion Engines and Emission Control, Seybothstraße 2, 93053 Regensburg, Germany
2   Scale MT GmbH, Franz-Mayer-Straße 1, 93053 Regensburg, Germany
*   Correspondence: florian1.zacherl@oth-regensburg.de

Abstract: Non-road sectors, such as agriculture and construction machinery, require high energy densities and flexibility in use, which is why diesel engines are mainly used. The use of climate-neutral fuels, produced from renewable energies, such as Oxymethylene Ether (OME) as a diesel substitute, can significantly reduce CO_2 and pollutant emissions in these sectors. In addition to CO_2 neutrality, OME also offers improved combustion characteristics compared to diesel fuel, eliminating the soot–NO_x trade-off and thus enabling new opportunities in engine design and calibration. In this paper, the combustion of pure OME on a close-to-production, single-cylinder non-road diesel engine with a pump–line–nozzle injection system is analyzed. A variation of the center of combustion at constant power output was performed for diesel and OME at different operating points. Two injectors were investigated with OME. A study on ignition delay and a detailed thermodynamic analysis was carried out. In addition, the exhaust emissions CO, NO_x, *VOC*, as well as particulate-matter, -number and -size distributions were measured. With OME, a significantly shorter ignition delay as well as a shortened combustion duration could be observed, despite a longer injection duration. In addition, the maximum injection pressure increases. *VOC* and CO emissions are reduced. Particulate matter was reduced by more than 99% and particle number (>10 nm) was reduced by multiple orders of magnitude. The median of the particle size distribution shifts from 60 to 85 nm (diesel) into a diameter range of sub 23 nm (OME). A significant reduction of NO_x emissions with OME enables new degrees of freedom in engine calibration and an efficiency advantage without hardware adaption.

Keywords: Oxymethylene Ether (OME); alternative fuel; diesel; pump–line–nozzle; soot; particles; NOx; pollutants; non-road application

1. Introduction

In the non-road sector, high requirements are set on the robustness, cost, flexibility and ease of handling of the machines, which is why mainly robust and cost-effective diesel engines are used in construction machinery. Stricter pollutant emission limits and the need to drastically reduce carbon dioxide (CO_2) emissions to limit global warming to 1.5 °C [1] require alternative solutions for applications where high energy densities are required and electrification is impossible [2]. Here, synthetic Power-to-Liquid fuels (PtL) produced from renewable energy sources with improved combustion properties compared to fossil fuels can make a significant contribution. The main feedstock for the synthesis of various PtL fuels is methanol (MeOH, CH_3OH), which could be produced from hydrogen (from electrolysis of water (H_2O) with electricity from renewable energy sources) and CO_2 (from industry process or direct air capture) [3,4]. Using non-fossil CO_2 sources and renewable energy creates a closed carbon cycle in the atmosphere with no impact on global warming.

The synthetically producible C1-oxygenates (Poly) Oxymethylene Dimethyl Ethers (OME_n) (molecular formula CH_3-O-$(CH_2$-O$)_n$-CH_3) are particularly well suited for the use

in compression ignition engines because of good ignitability and their physico-chemical properties (especially $n = 3$–5) [5–7]. The OME_n chains are synthesized either by a route from MeOH and formaldehyde (FA, CH_2O) with dimethoxymethane and trioxane as intermediates or by direct synthesis from MeOH and FA with the formation of H_2O [5,8–10]. The OME production costs of the second synthesis route are lower, which is why it has recently received more attention [10,11].

Since the physical and chemical properties of the individual OME_n molecules differ greatly, the combustion properties of an OME mixture (OME_{Mix}) strongly depend on its composition from the individual components. In order to enable the introduction of OME fuel into the market, the technical specification DIN/TS 51699 is going to be defined [12]. DIN/TS 51699 defines the limits for important properties such as freezing point, cetane number, oxidation stability and flash point. The defined mixture consists primarily of OMEs with a chain length from 3 to 5 ($OME_{3–5}$) and only a small amount of OME_6 [12].

Due to the oxygen content in the molecular structure of OME and the lack of C–C bonds between the atoms, numerous studies with pure OME_n and mixtures of different OME_n chains have shown that the nitrogen oxide (NO_x)–soot trade-off, common for diesel engines, does not exist [13–24]. Similarly, studies on OME and diesel blends show a significant reduction in soot emissions due to the increasing amount of oxygen in the blend, with a nonlinear relationship between blend rate and soot reduction [23,25–29].

In particle formation, soot precursors such as acetylene play a crucial role, as these combine to form polycyclic aromatic hydrocarbons (PAHs), growing in turn into larger soot particles, which is why the formation rate of the first PAH rings decisively determines the total soot mass [30]. Gaiser et al. [31,32] found that in OME combustion, due to the lack of C–C bonds, no typical soot precursors are formed, even under fuel-rich conditions, and mainly oxygenated species participate in the reaction. Furthermore, the influence of chain length on the species pool occurring during the reaction [31,32], reaction kinetics [33] and particle formation [34] seems negligible. Extensive studies on the laminar flame velocity, ignition behavior and reaction kinetics of OME combustion were carried out in [31–42]. The combustion process of OME and soot formation in injection sprays was studied in detail using optical methods in [43–48]. On engine experiments with OME, it was shown that the particle size distribution (PSD) shifts to particles with a mobility diameter (D_P) of <23 nm (nucleation mode) [21,29,49–52]. Due to the complex conditions in a combustion chamber (flow, pressure, temperature,...), the cause and mechanisms of particle formation, as well as their composition, are not yet fully understood, so further research is needed.

Previous investigations with OME have mainly been carried out on engines with modern common-rail injection systems, elaborate exhaust gas aftertreatment systems, exhaust gas recirculation (EGR) options and turbocharging. In strongly cost-driven engines without these options and with rudimentary injection technology, the fuel represents the greatest and in some cases the only lever for reducing pollutants and increasing efficiency. The excellent combustion properties of OME allow an omission of multiple injections and a reduction of injection pressure without any disadvantages in particulate or NO_x emissions, whereby a simplification of the injection system and the exhaust gas aftertreatment system seems possible [16,19,20].

Therefore, the aim of this work is to investigate the potentials of OME on a low-cost close-to-production naturally aspirated non-road diesel engine with a pump–line–nozzle (PLN) injection system without EGR. This article shows the results from experiments with a OME_{3-6} mixture (further only called OME) and diesel as a reference. The influence of a variation of the center of combustion (COC) on NO_x, particle number (*PN*), particulate matter (*PM*), volatile organic compounds (*VOC*) and carbon monoxide (CO) formation, particle size distribution (PSD), combustion noise, efficiency (η) and ignition delay (τ_{ign}) is shown for OME and diesel at two different operating points (OP). The results of the variation of the COC are subjected to a detailed thermodynamic analysis with consideration of friction and heat losses. For OME, the influence of two nozzles with different injection rate curves on combustion and the influence of physical properties of OME on the

hydraulics of the PLN injection system is discussed. An approach for the more accurate determination of ignition delay using a needle lift sensor on the engine is presented, and the results are shown using the series nozzle as an example. Finally, the potential for efficiency improvement through calibration as a result of reduced NO_x emissions with OME is discussed for the close-to-production engine.

2. Materials and Methods

2.1. Tested Fuels

All reference measurements have been performed with fossil diesel fuel, which fulfills the requirements of EN 590 [53]. The exact composition of the investigated OME ($n = 3$–6) and other properties of both fuels can be found in Table 1.

Table 1. Selected fuel properties of diesel according to EN 590 and the test fuel OME-Mix 3–6 used for this study.

	Diesel EN 590 [a]	OME [b]	Unit
Lower Heating Value (LHV)	42.45	19.20	MJ/kg
Density (ρ) @ 40 °C *	825.5	1040.7	kg/m^3
Oxygen content	1.1	47.0	%(m/m)
Carbon content	85.3	43.6	%(m/m)
Air–fuel ratio (AFR)	14.40	5.95	kg$_{Air}$/kg$_{Fuel}$
Diesel equivalent	1	1.75	m^3/m^3
AFR/LHV	0.339	0.310	kg$_{Air}$/MJ
CO_2 factor	265	299	g$_{CO_2}$/kWh
H_2O factor	103	145	g$_{H_2O}$/kWh
Cetane number (CN)	>51 [53]	70	-
Flash point	>55 [53]	64	°C
Boiling range	170–390 [53]	157–273 [54]	°C
Speed of sound (c) @ 40 °C and 45 bar **	1297	1193	m/s
Bulk modulus (K) @ 40 °C and 45 bar ***	1.39	1.48	GPa
Kin. viscosity (ν) @ 40 °C	2.0–4.5 [53]	1.18	mm^2/s
HFRR	<460 [53]	390	μm

[a] Diesel fuel according to EN 590 with 7% FAME [53]. [b] Mixture composition [wt.%]: 47.76 % OME_3, 29.58 % OME_4, 16.38 % OME_5, 5.32 % OME_6. * Measured with density meter DMA 35 from Anton Paar GmbH. (5–45 °C). $\rho_{Diesel} = -0.0007T + 0.8535$, ($R^2 = 0.9994$); $\rho_{OME} = -0.0008T + 1.0727$, ($R^2 = 0.9935$). ** Measured with HDA injection rate analyzer from Moehwald GmbH, Homburg. *** Calculated with $K = c^2\rho$. Assumption $\rho_{45bar} \approx \rho_{1bar}$ and rigid line.

The investigated diesel is a standard gas station B7 fuel, including 7% Fatty Acid Methyl Esters (FAME). Important parameters such as lower heating value (LHV) as well as the oxygen and carbon content in Table 1 have been determined with an analysis for both fuels. The significantly higher oxygen content of OME leads to a reduced LHV compared to fossil diesel fuel. The higher density of OME can only partially compensate this disadvantage, which is why 1.75 times the volume (diesel equivalent) must be injected to achieve the same power output. Some important properties such as cetane number (CN), boiling range and lubricity (High-Frequency Reciprocating Rig, HFRR) are within the limits of EN 590, allowing the fuel to be used in conventional diesel engines and their injection systems. The CN of OME is well above the EN 590 limit (CN > 51), which improves the fuel ignition process. OME_{3-6} has a lower viscosity than diesel fuel. For the given values of the bulk modulus, it must be taken into account that this is a simplification, since the density and the bulk modulus are temperature and pressure dependent. In addition, stiffnesses in the system were not taken into account.

2.2. Experimental Setup

2.2.1. Test Engine

All measurements have been performed at a close-to-production single-cylinder non-road diesel engine. It is naturally aspirated and has a PLN injection system. The parameters of the engine are shown in Table 2.

Table 2. Parameters of the test engine.

	Value	Unit
Number of cylinders	1	-
Displacement	347	cm^3
Bore/Stroke	80/69	mm
Compression ratio	21.5:1	-
Max. Power @ 3600 1/min	4.5	kW
Max. Torque @ 2100 1/min	14.7	Nm
Range of speed	1000–3600	1/min
Type of cooling	Air cooled	-
Injection system	pump–line–nozzle	-
Exhaust gas recirculation	no	-
Engine charging	Naturally aspirated	-

Some adjustments must be made to the series engine for test bench operation. The cylinder head installed in the series engine contains a bypass that allows exhaust gas to flow from the exhaust side to the intake side. This enables an engine speed and load dependent but uncontrolled EGR and reduces NO_x emissions. To eliminate the influence of uncontrolled EGR, a cylinder head without an EGR bypass is mounted. The generator integrated in the series engine is removed and the engine control unit (ECU) is powered via an external voltage source in order to minimize external influences and uncontrolled parasitic losses. To avoid cross-influences, functions implemented in the series ECU software, such as quantity correction in cold start, are deactivated. Furthermore, the diesel oxidation catalyst is replaced by an empty silencer to enable an engine-out emission measurement.

2.2.2. Fuel and Injection System

Due to the need of fuel consumption measurement and the repeatedly observed material incompatibilities between OME and commonly used elastomers in diesel engines, such as flourine rubber (FKM), the low-pressure circuit of the fuel system must be adapted [16,17,19,55]. The reason for the incompatibility to certain elastomers is the oxygen bond in the OME molecule and the resulting dipole moment, which makes OME a strongly polar solvent [56]. In contrast, the hydrocarbon chains of diesel fuel are non-polar. Substances with the same polarity dissolve into each other, which is why the polar OME dissolves in the polar FKM, resulting in increasing volume and mass. The elastomers propylene diene rubber (EPDM) (non polar) and the chemically very resistant materials perfluoroelastomers (FFKM) and polytetrafluoroethylene (PTFE) are suitable for OME operation, but EPDM is not suitable for use in diesel fuel because of its polarity, and FFKM is a very expensive material [19]. Therefore, all fuel-carrying hosepipes are exchanged to PTFE for the test bench operation, and the fuel tanks are replaced by stainless steel tanks with compression fittings. The schematic layout of the fuel system and the engine test bench with all measurement systems can be seen in Figure 1.
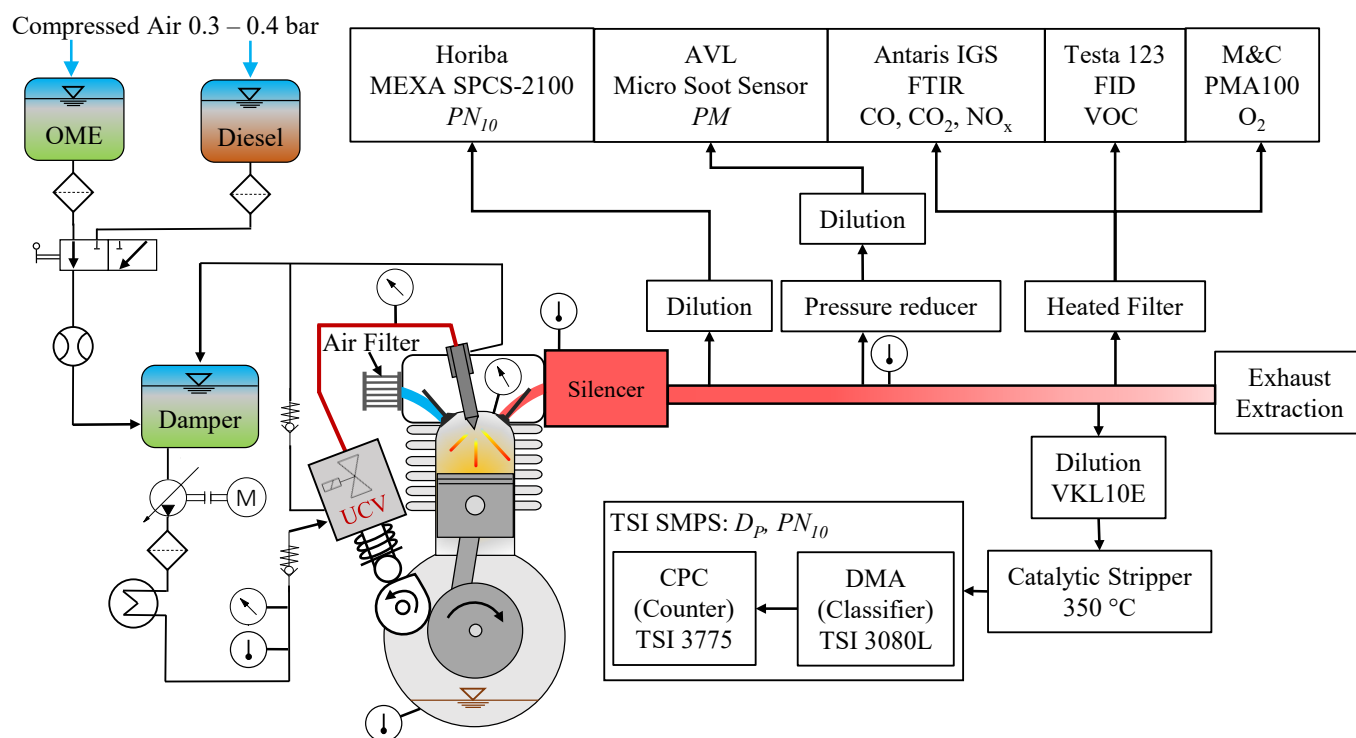
Figure 1. Schematic layout of the fuel system and the engine test bench with all measurement systems.

The two fuel tanks are pressurized with compressed air at a constant pressure of 0.35 bar, and the outflowing fuel is then pre-filtered. After a changeover valve, the fuel flows through a coriolis flow meter (Section 2.2.3) into a compensating volume. The compensating volume is partially filled with air and serves to dampen pulsations in the low-pressure circuit. The pre-feed pump regulates the fuel pressure upstream of the high-pressure pump (HPP) to a pressure of 0.5 bar, and the fuel is then filtered and conditioned in a heat exchanger to a temperature of 35 °C. Two check valves prevent back-flow of the fuel.

The injection system is an electronically controlled pump–line–nozzle system. Here, the pump piston of the HPP is driven by a camshaft. As long as the Unit Control Valve (UCV) of the HPP is not actuated by the ECU, the system delivers the fuel to the return line of the low-pressure circuit. During actuation, the solenoid valve shuts off the flow to the return, causing the pump piston to build up pressure in the high-pressure path. As soon as the opening pressure of the hydraulically actuated injector is reached, injection begins. After the UCV is switched off, the pressure in the high-pressure path is relieved via the low-pressure side, the injector is closed, and injection is thus terminated. Thus, by adjusting the energizing time of the solenoid valve (*TOE*), the injection mass can be controlled depending on the engine load and speed.

In this work, two different injectors with a different injection rate curve in OME operation are investigated. The first nozzle is the rate-shaping (RS) nozzle used in the production engine, and the second nozzle is a proportional-opening (P) nozzle. The RS-nozzle is equipped with a needle lift sensor (Section 2.2.3) for the OME and diesel measurements. The injection rate curves and the injected energy of the two nozzles are shown as an example for an operating point with identical injection parameters in Figure 2 and were recorded with an HDA injection rate analyzer from Moehwald GmbH. The P-nozzle shows a nearly rectangular shape of the injection rate, whereas the RS-nozzle limits the flow during the opening process (Rate Shaping) and shows a pronounced increase in the injection rate during the closing process (Post-Spray). The limited flow during the nozzle opening of the RS-nozzle acts as a kind of pre-injection and is intended to reduce exhaust and noise emissions during diesel operation. The higher mass flow through the RS-nozzle

with OME can be explained by the higher density of OME compared to diesel. Due to the higher bulk modulus and the lower viscosity of OME (Table 1), a slight elongation of the injection duration occurs for the RS-nozzle, despite the same *TOE* [57,58]. With the normalized injected energy in Figure 2b, it can be seen that due to the lower LHV of OME, significantly less energy is injected for both nozzles for the same solenoid valve actuation time. The P-nozzle injects more mass for the same actuation time, but not enough to fully compensate the difference in LHV between OME and diesel. Therefore, the *TOE* needs to be extended with OME.
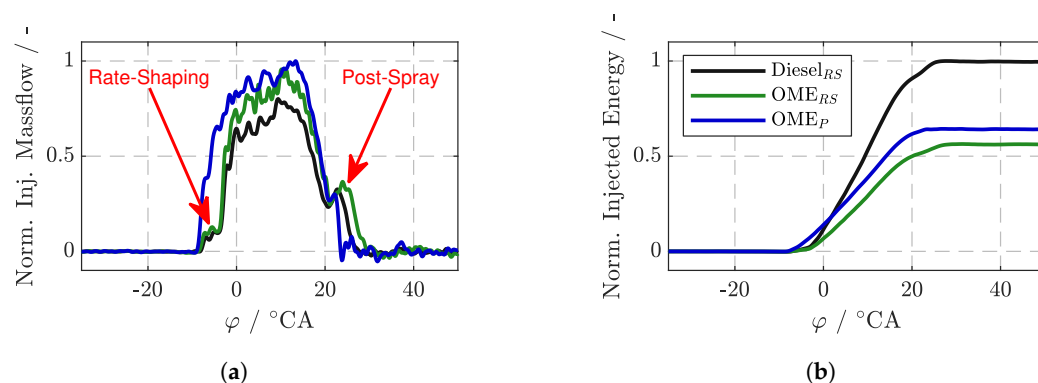

(a)   (b)

Figure 2. Example of normalized injection rate (**a**) and normalized injected energy (**b**) for RS− and P−nozzle at $n = 2640 \, 1/\text{min}$, $TOE = 1950 \, \mu\text{s}$ and $SOE = 26.5 \, °\text{CA BTDC}$.

2.2.3. Measurement Systems

A schematic overview of the used measurement systems can be seen in Figure 1. The fuel consumption is determined with a coriolis flowmeter SITRANS F C MASSFLO of the type MASS 2100 DI 1.5 from Siemens AG. For needle lift measurement of the RS-nozzle, an eddy current displacement sensor of type EU05(66) and an EA3200-EU05(66)M matching board with a DT3300 controller from Micro-Epsilon Messtechnik GmbH & Co. KG (Ortenburg, Germany) are used.

The entire measuring chain for pressure acquisition on the test stand is set up with sensors from Kistler Instrumente GmbH. To measure the cylinder pressure, a piezoelectric pressure sensor of type 6056A is positioned in the combustion chamber with the aid of a glow plug adapter of type 6542Q. The charge signal generated by the sensor is amplified by a charge amplifier of type 5064C in a signal conditioning platform of type SCP2853 and converted into a voltage signal. The pressure in the injection line is measured by a type 4067E sensor with a measuring range up to 2000 bar which is mounted on the injection line 225 mm before the injection nozzle with a clamp adapter of type 6533A11. All high-resolution signals are acquired with an IndiModul Gigabit from AVL List GmbH and processed with a resolution of 0.1° crank angle (CA). For the combustion analysis, 200 consecutive operating cycles are recorded and averaged per measurement point.

To ensure that the sample gas is taken evenly over the entire exhaust pipe diameter, multi-hole probes with an internal pipe diameter of 6 mm are used for exhaust gas sampling. In total, the multi-hole probe contains 15 holes with a diameter of 1.5 mm, which means that the total cross-section of all holes (26.5 mm^2) corresponds approximately to the cross-section of the 6 mm sampling tube (28.3 mm^2). The 15 holes are arranged in three rows of five holes each at a 120° angle to each other.

A solid particle counting system (SPCS) type MEXA 2100 from HORIBA Europe GmbH is used to measure the *PN* down to a diameter of 10 nm. It contains a condensation particle counter (CPC) of the type CPC-100 manufactured by the TSI GmbH. The sample gas is prepared in three dilution stages, and an evaporation tube heated up to 350 °C is used to remove volatile components. As standard, the CPC achieves a counting efficiency of 50% (±12%) at 23 nm (±1 nm). By increasing the saturator temperature inside the CPC from 38.5 to 39.2 °C and reducing the condenser temperature from 30.8 to 21.2 °C, the counting efficiency could be increased to 52.6% for a mobility diameter of 10 nm and

improved to nearly 100% for particles >30 nm [59]. For diesel measurements, a dilution factor of 2000 is set, and for OME, a dilution factor of 200 is set.

PM measurements are performed by using a Micro Soot Sensor (MSS) from AVL List GmbH, which works on a photoacoustic measurement principle. The raw exhaust gas is sampled with a multi-hole probe, and a pressure reduction unit is installed to dampen the pressure pulsations of the single cylinder engine. The dilution factor of the internal dilution unit is set to 20 for the diesel measurements and is set to two for the OME measurements. Since the measuring cell temperature of the MSS is 52 °C and the exhaust gas cools down between the extraction point (T_{EP}) and the MSS, a correction of the measured value according to Kittelson and Johnson [60] is applied to consider the particle losses due to the thermophoretic effect (Equation (1)).

$$PM_{Kittelson} = PM_{MicroSoot} \cdot \left(\frac{T_{EP} + 273.15 \text{ K}}{52 \text{ °C} + 273.15 \text{ K}} \right)^{0.38} \tag{1}$$

To determine the particle size distribution (PSD), the sample gas is first taken from the exhaust pipe using a multi-hole probe and then diluted by a VKL 10E dilution unit from Palas GmbH at a ratio of 1:10. Subsequently, volatile components are oxidized at 350 °C by using a Catalytic Stripper CS010 (CS) from Catalytic Instruments GmbH & Co.KG. In the Catalytic Stripper, losses occur due to diffusion processes and thermophoresis, especially with small particles, which is why the manufacturer provides a particle loss curve for this device [61]. Despite higher particle losses in the sub 10 nm range, a Catalytic Stripper, consisting of an evaporation tube or thermodenuder, is recommended, because of a better handling of semi-volatile concentrations [62]. In this paper, the measured values of particle size distribution are not corrected and are shown as measured. Following the CS, the sample gas enters a scanning mobility particle sizer (SMPS) manufactured by TSI GmbH. This sizer consists of a Type 3087 aerosol neutralizer, a Type 3080L electrostatic classifier (longest version of the differential mobility analyzer (DMA)) and a Type 3775 condensation particle counter, where particle diameters between 6 and 217 nm are measured. The error bars of the PSD show the standard deviation for 16 measurements with diesel and 34 measurements with OME at a daily check reference point. The measurements have been performed at different dates and between the *MFB* 50% variations.

The gaseous components CO, CO_2, NO, NO_2 are measured by using a Fourier Transform Infrared Spectrometer (FTIR) of type Antaris IGS from Thermo Fisher Scientific Inc.. A Testa 123 flame ionization detector (FID) from Testa GmbH determines the *VOC*, and a paramagnetic detector of the type PMA100 from M&C is used for measurements of the oxygen (O_2) content. When measuring oxygen-containing molecules (C1 structure of OME) with the FID, a response factor smaller than 1 needs to be considered [63].

2.3. Test Methods

Table 3 shows the operating points (OP) of the engine tests. At each OP, the engine is controlled to constant speed (*n*) and break mean effective pressure (*BMEP*). At constant *BMEP*, the INCA application software was used to adjust the start of energizing (*SOE*) until the angle at which 50% of the injected fuel mass is burned (*MFB* 50%), also called center of combustion (COC), matches the values shown in Table 3. The test stand controller adjusts the foot pedal position, and thus the *TOE*, until the *BMEP* remains constant. The variation limits of the *MFB* 50% are given by a maximum cylinder pressure of 70 bar and an unstable combustion at late *MFB* 50% positions. Therefore, at high loads and speeds, the number of measurement points must be reduced. Due to hydraulic instabilities and the resulting unstable combustion when using the P-nozzle, the measurement point with *MFB* 50% = 8.1 °CA ATDC at OP_1 could not be recorded. The reasons for this behavior could be the increased stiffness in the low-pressure circuit due to the conversion to PTFE pipes, the lower compressibility of OME and a lack of tuning of the P-nozzle to the standard injection system. The location of the investigated OPs in Non-road Transient Cycle can be seen in Figure 3.

Table 3. Investigated operating points and values of *MFB* 50% variation.

	Meas. No.	OP_1	OP_2	Unit
n		2600	3300	1/min
BMEP		2.2	3.8	bar
MFB 50%	1	8.1	13.8	°CA ATDC
	2	10.0	16.2	°CA ATDC
	3	11.8	19.0	°CA ATDC
	4	14.0	21.7	°CA ATDC
	5	16.9	-	°CA ATDC
	6	23.9	-	°CA ATDC
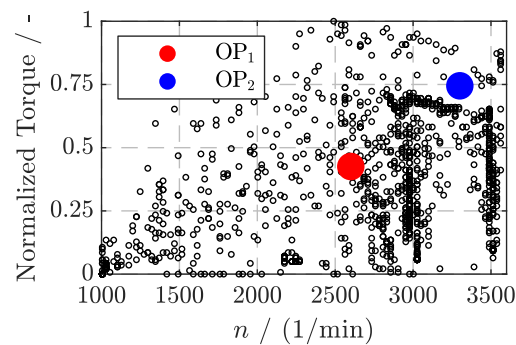
Figure 3. Location of the investigated operating points in Non-Road Transient Cycle.

The time-based measurement data are recorded over a time period of 30 s. Due to strong pipe oscillations in the cylinder pressure signal, the frequency range of 8500–16,500 Hz is filtered out by using a bandstop filter. This frequency range has been determined as the cause of the pipe oscillation via a fast Fourier transformation (FFT). Furthermore, a moving average filter is applied to the cylinder pressure signal with a window length of 1 °CA. The integration boundaries for the calculation of the normalized cumulative heating curve (Q_{Norm}) are set from −15 to 90 °CA. The ignition delay (τ_{ign}) is determined by using the needle lift sensor and the 5% turnover point of the cumulative heating curve (*MFB* 5%). Here, the start of injection (*SOI*) is set when the 10% value of the maximum needle lift is reached. The advantage of a needle lift sensor is that the hydraulic opening delay of the injection system is excluded in the calculation, and thus, the ignition delay can be determined more precisely. The ignition delay in µs can be calculated with Equation (2), where *n* is the engine speed in 1/min.

$$\tau_{ign} = \frac{MFB\ 5\% - SOI}{6n}10^6 \tag{2}$$

The air–fuel equivalence ratio (λ) is calculated with the Brettschneider formula [64]. The friction mean effective pressure (*FMEP*) is calculated from the measured indicated mean effective pressure (*IMEP*) and the *BMEP*.

$$FMEP = IMEP - BMEP \tag{3}$$

3. Results and Discussion

3.1. Thermodynamic Combustion Characteristics

3.1.1. Operating Point 1

First, the thermodynamics of OME combustion and the injection system behavior are discussed in order to draw conclusions about the emissions and their formation. In Figure 4, the drive current of the UCV (I_{UCV}), the pressure in the injection line (p_{inj}), the cylinder pressure (p_{cyl}), the rate of heat release (*RoHR*), and the cumulative energy (Q_{norm}) normalized to the total amount of energy injected are shown for two selected *MFB* 50% at OP_1 as a function of the crank angle (φ). The solid lines relate to a COC closer to the top

dead center (TDC) (MFB 50% = 10.0 °CA), whereas the dashed lines represent an OP with late COC (MFB 50% = 23.9 °CA). Table 4 lists the measured values of the most important variables for the shown OPs and the respective combustion centers.
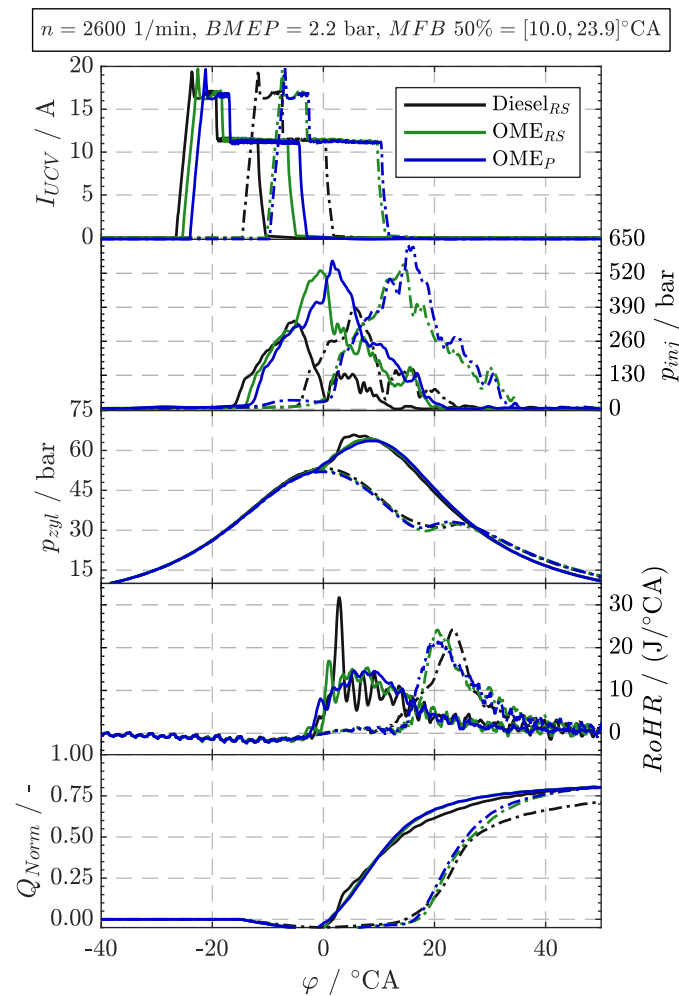

Figure 4. Drive current of high−pressure pump solenoid valve, pressure in injection line, cylinder pressure, rate of heat release and normalized released heat as a function of crank angle at two different MFB 50% timings for OP_1 and for two different nozzles in OME operation. Solid lines MFB 50% = 10.0 °CA, dashed lines MFB 50% = 23.9 °CA.

Table 4. Additional measurement values of OP_1 corresponding to Figure 4.

OP_1	TOE μs		SOE °CA BTDC		η_i %		$FMEP$ bar		MFB 5% °CA ATDC		BD_{5-90} °CA		BD_{50-90} °CA		$p_{inj,\,max}$ bar	
$\frac{MFB\ 50\%}{°CA\ ATDC}$	10.0	23.9	10.0	23.9	10.0	23.9	10.0	23.9	10.0	23.9	10.0	23.9	10.0	23.9	10.0	23.9
$Diesel_{RS}$	964	990	27.0	15.0	45	37	1.60	1.58	1.20	14.2	32.8	32.9	23.8	22.9	335	386
OME_{RS}	1258	1320	25.9	10.5	45	40	1.58	1.56	0.80	16.0	25.9	24.4	16.9	16.4	527	550
OME_P	130l	1340	24.5	10.0	45	40	1.61	1.59	0.20	15.8	26.8	23.2	17.1	15.6	592	624

Looking at the drive current of the UCV for OP_1 (Figure 4), it is noticeable that the UCV for both nozzles in OME operation is controlled by about 1–2.5 °CA later than with diesel, although due to the lower LHV of OME, the TOE for the same effective mean pressure must be selected significantly longer overall, and the same center of combustion must be maintained (Table 4). At late COC, the UCV is actuated up to 5 °CA later for OME than with diesel. The injection pressure increases proportionally with actuation time in a

PLN injection system [65]. Therefore, due to the longer *TOE*, the maximum pressure in the injection line at this OP is ≈200 bar higher with OME for the RS-nozzle and ≈250 bar higher for the P-nozzle than with diesel. In addition, the higher peak pressure and a slightly steeper increase in pressure in OME operation is due to the higher bulk modulus of OME (Table 1).

With diesel, there is a drop in the pressure of the injection line for both COC, which is followed by a rise shortly after the UCV is turned off. In the case of OME, the pressure in the injection line decreases continuously after shutdown. The pressure curve in a PLN system depends significantly on the position of the pressure sensor, the *TOE*, the wave impedance of the injection line (diameter, length, injector geometry), the bulk modulus, the speed of sound, the density of the fuel, and many other factors [65]. In the pipe, the pressure wave generated by the pump piston is reflected several times, causing location-dependent interference and cancellation phenomena, and thus, the injection pressure at the nozzle outlet differs from the pressure measured in the pipe, and the latter has a phase shift. This, and the operation of the RS-nozzle in the ballistic range with diesel could be a reason for the different pressure drop. The higher pressure of the P-nozzle is mainly due to a different opening pressure of the nozzle and the changed wave impedance of the injection system due to the changed nozzle geometry.

Looking at the cylinder pressure and *RoHR* (Figure 4), it can be observed that the pressure curve with diesel and at early COC positions (*MFB* 50% = 10.0 °CA) shows a steeper gradient, and the peak pressure is about three bar higher compared to OME. This is due to about twice the maximum heat release during the pronounced premixed combustion phase with diesel. With OME, an only moderately pronounced premixed phase occurs for the RS-nozzle, and no premixed combustion phase occurs for the P-nozzle because of a shorter ignition delay. The RS-nozzle initially shows a low heat release for OME and diesel, as in a type of pre-injection with a subsequent steep increase in the conversion rate. The reason for this is the throttled injection rate during the rate-shaping phase. With the P-nozzle, the *RoHR* rises immediately. For OME, the *RoHR* increases for both nozzles during the diffusion combustion phase, which is due to the rising injection pressure and thus increasing mass flow rate during injection because of the extended *TOE*. Therefore, for both nozzles, despite the lower LHV of OME, the heat release per crank angle is higher during the diffusion combustion phase than during diesel combustion. As a result, the lower LHV of OME can partly be compensated, and a reduced burn duration ($BD_{5–90}$) can be observed with OME despite a significantly longer actuation time (Table 4). The shorter burning duration is due to the higher CN and oxygen bond in the molecular structure of OME. In the normalized cumulative heating curve of the *MFB* 50% = 10.0 °CA point, it can be seen that more heat is initially released during diesel combustion due to the high premix fraction and LHV, but OME combustion is completed much earlier overall. A faster burnout ($BD_{50–90}$, Table 4) can be explained by the reduced soot formation with OME during the main combustion phase which results in less soot to be oxidized in the later combustion phase [66]. Previous findings showed that oxygenated fuels burn faster due to higher oxidation rates, which is consistent with these measurement results [67,68]. The friction *FMEP* and the *IMEP* are almost the same for both nozzles and fuels.

The OP with a very late COC (*MFB* 50% = 23.9 °CA) shows a completely different combustion behavior than the OP with a center of combustion closer to TDC. The maximum cylinder pressures occurring during combustion are approximately the same, and the pressures in the injection line are slightly increased for all three nozzles and fuel combinations due to a longer *TOE* compared to the OP with an early center of combustion (Table 4). The reason for the elongation in *TOE* is the reduced efficiency at late COC. For *RoHR*, a similar pattern occurs for all fuels and nozzles, showing high conversion rates and no classical diffusion-controlled combustion phase. Due to the late injection in the expansion phase, the mixture formation process is affected because of low temperatures in the cylinder, low turbulence in the charge movement and the low back pressure, which increases the ignition delay time and results in the formation of a partially homogenized mixture in

the combustion chamber. This mixture burns at a high conversion rate after auto-ignition. Diesel combustion starts earlier than OME combustion, but it rises to its maximum at a much flatter rate than OME combustion because of lower oxidation rates (no oxygen in molecule). The earlier start of combustion with diesel can be explained by the 5 °CA earlier *SOE* and the associated earlier injection for the same COC. Even with a very late COC, the OME combustion is completed significantly earlier than with diesel. In addition, the total amount of energy converted is significantly lower with diesel, which can be attributed to incomplete combustion and high heat losses due to a long combustion period with a large combustion chamber surface and thus leads to a reduction of the indicated efficiency (η_i) by 3 percent points compared with OME. Overall, the differences in the *RoHR* between the two nozzles with OME can be considered to be small. Due to the short ignition delay and the lower LHV of OME, the rate-shaping phase plays a minor role and the effect of RS injection rate on the combustion process seems to be negligible. In addition, the maximum nozzle flow rates differ only slightly.

In order to analyze the differences in burning duration, indicated efficiency, friction and heat losses in more detail, Figure 5a–d are used. Figure 5a shows the ignition delay for OME and diesel and the RS-nozzle at OP_1 as a function of *SOI*. OME shows a shorter τ_{ign} for all points compared to diesel. In addition, a strong dependence on injection timing relative to TDC is observed for diesel, whereas this dependence is much less for OME. If the fuel is injected very early in the compression phase, the cylinder pressure and temperature are not yet at their maximum, which means that jet breakup and fuel evaporation take more time, thus increasing the ignition delay. During the compression phase, however, sufficient charge movement due to swirl and squish flow in the piston bowl favors mixture formation, resulting in a shorter τ_{ign} for injections before TDC than after TDC. In the expansion phase, pressure and temperature decrease continuously, and the kinetic energy of the cylinder charge is reduced, which is why significantly longer ignition delay times occur with injections beginning ATDC. For diesel, a clear minimum of τ_{ign} is shown at 4–6 °CA before TDC. It is assumed that the turbulence level in the piston bowl is highest there due to squish flows, whereby mixture formation is affected positively. Shimamoto and Akiyama [69] showed for a cylindrical piston bowl and different piston bowl diameter to bore ratios that the maximum squish velocity occurs at about 5–10 °CA BTDC (losses neglected). However, the mixture formation and flow processes in the combustion chamber are very complex and strongly depend on the piston bowl and combustion chamber geometry. The significantly reduced dependence of the τ_{ign} on the *SOI* with OME is due to the improved ignition properties resulting from the higher CN, the lower boiling point and, above all, the oxygen content in the molecular structure. Due to the intrinsic oxygen bond, the influence of the charge movement on the mixture formation processes decreases, since the oxygen required for combustion is carried along in the molecule and does not have to be supplied from the charge air by air entrainment [70]. This enables the combustion to be located closer to the nozzle tip, where the turbulence level is higher [70]. Since the opening pressure of the RS-nozzle remains constant for both fuels, the injection pressure before the start of combustion is relatively similar. However, it should be noted that at the same injection pressure, OME has a lower nozzle outlet velocity and thus a lower momentum flux compared to diesel due to its higher density [71,72], resulting in less turbulence being introduced into the combustion chamber at this time. Pöllmann et al. [73] observed on an optically accessible single-cylinder diesel engine with a common-rail-injection system that the ignition delay of the OME_{3-6} investigated there is almost independent of the injection pressure and the nozzle geometry, but it is prolonged at low cylinder pressure at the *SOI*.
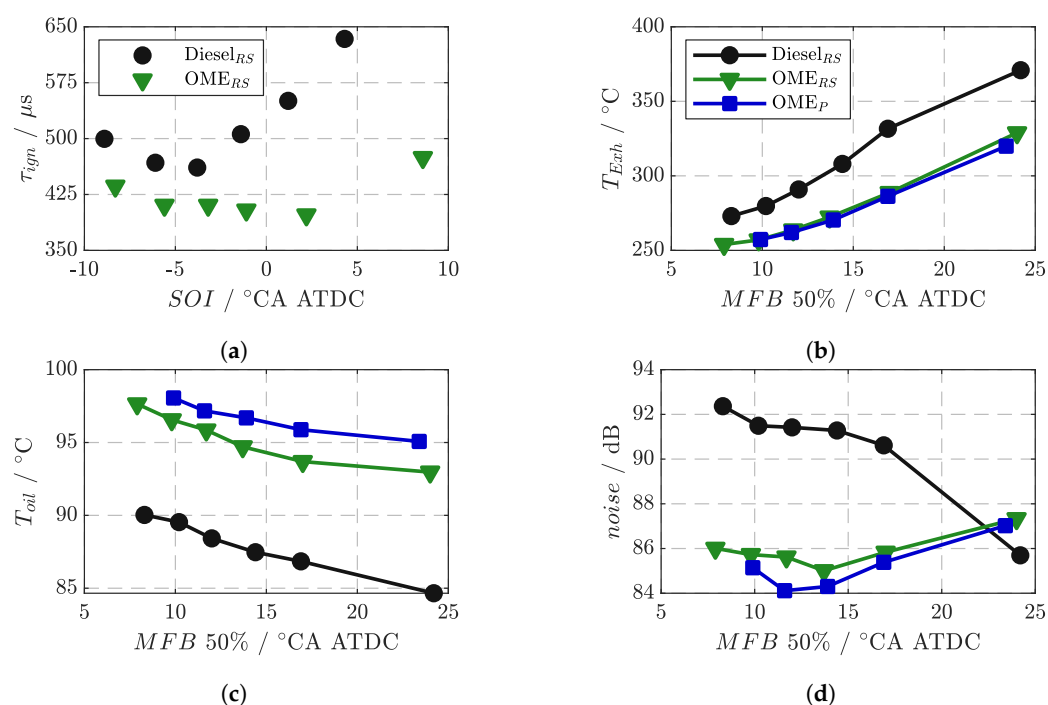
Figure 5. Ignition delay ((**a**), calculated with needle lift sensor of RS−nozzle), exhaust gas temperature (**b**), oil temperature (**c**) and combustion noise (**d**) for a variation of *SOI* (**a**) or *MFB* 50% (**b**–**d**) at OP$_1$ ($n = 2600$ 1/min, *BMEP* = 2.2 bar) for two different nozzles in OME-operation.

Figure 5b shows the exhaust gas temperature (T_{Exh}) for OP$_1$ as a function of *MFB* 50%. The exhaust gas temperature increases with later positions of the COC, since the heat of combustion in the working process cannot be converted into mechanical work efficiently, which significantly decreases the indicated efficiency (Table 4). The lower exhaust gas temperature of OME is due to the higher exhaust gas mass flow because of the larger injection mass and the significantly higher heat capacity due to a higher concentration of water vapor and CO_2 in the exhaust gas (CO_2 and H_2O factor in Table 1). At later COC positions, the gap in exhaust gas temperature between OME and diesel combustion increases, since OME has a significantly shorter burning duration and faster burnout due to its oxygen content, resulting in more efficient combustion. Especially at late COC positions, a shorter combustion duration ensures lower wall heat losses. A further small effect for lower exhaust gas temperatures could be the slightly higher value for enthalpy of vaporization of OME [18].

With OME, significantly higher oil temperatures were measured on the air-cooled engine than with diesel, despite the same ambient temperature and same fan speed (equal to the engine speed) of the engine cooling system (Figure 5c). During the measurement campaign, the combustion chamber was regularly inspected with an endoscope to identify possible damage. It was found that during diesel operation, there were heavy soot deposits on the piston crown, whereas in OME operation, no soot deposits were visible and the piston was metallic bright. As already proven several times, very low *PM* emissions are generated during OME combustion [15–17,50], which is why a buildup of soot depos2tions on engine components is not to be expected during OME operation. Existing soot deposits were oxidized after switching from diesel to OME operation, thereby cleaning the combustion chamber independently. The prolonged injection due to the reduced LHV leads to a longer interaction of the flame front with the piston bowl, which is expected to result in a higher heat input. An impingement of the burning spray with the piston bowl leads to higher local surface heat flux [74]. Higher wall temperatures on the piston lead to a reduction or complete removal of soot deposits on the piston, even in diesel operation [75]. In addition, the soot layer in the combustion chamber acts as an insulator, which is why a higher heat flux occurs in the absence of deposits and thus more heat is

transferred to the piston [75,76]. The heat flux is strongly dependent on the composition of the depositions and therefore from the used fuel [76]. Approximately 50% of the energy leaving the closed cylinder system goes through the piston and approximately 30% goes through the cylinder head [77]. The energy supplied to the piston is transferred to the engine oil via the piston rings, causing the oil temperature to rise. Another effect could be that due to the higher injection pressure with OME, a longer jet penetration length occurs, and thus, the combustion takes place predominantly near the piston wall. Furthermore, more kinetic energy is introduced into the combustion chamber by the fuel system due to the higher total mass flow (lower LHV), thus increasing the turbulence level [20], which could further increase the heat transfer coefficient and thus increase heat losses. In contrast, the absence of soot during combustion and a reduced adiabatic flame temperature of OME could reduce the heat losses through radiation, but these processes are very complex and could not be further validated in terms of this work. The differences in oil temperature between the nozzles with OME are small.

The fact that the same indicated efficiency of 45% (Table 4) occurs for both nozzles and fuels in OME combustion at early COC despite a significantly shorter combustion period confirms that greater heat losses occur in OME operation. At first, the piston section is subjected to more stress due to the extended injection. Furthermore, more heat is extracted from the combustion chamber to evaporate the higher injection mass and due to the slightly higher values for enthalpy of vaporization of OME compared to diesel [18]. At late COC, diesel combustion efficiency decreases more severely than OME due to inadequate mixture formation and the longer $BD_{5–90}$. Surprisingly, the $FMEP$ at this OP is very similar for all COCs (Table 4), although the HPP requires significantly more energy to pump the higher fuel mass and to produce the higher injection pressure. It is assumed that the higher oil temperatures occurring in OME operation reduce the viscosity of the SAE 10W-40 engine oil and thus reduce friction in the crankshaft drive. This can compensate for the higher energy demand for fuel injection at this OP.

When considering the combustion noise as a function of the center of combustion in Figure 5d at OP_1, a strong dependence on the center of combustion becomes apparent for diesel, similar to the ignition delay, which is less pronounced for OME. The combustion noise was determined from the cylinder pressure curve by means of a noise analysis using the AVL INDICOM v2.6 software. Due to the lower premixing proportion at early COC positions and the resulting smaller pressure gradient in the cylinder pressure curve, the combustion noise in OME operation is reduced by up to 6 dB for both nozzles. This corresponds to a reduction in sound intensity by a factor of four, which significantly reduces the noise level in the environment of the engine. At very late COCs, both fuels and nozzles show similar noise levels, which can be attributed to the similar $RoHR$ and cylinder pressure curve with small pressure gradients. For early COC, the noise emissions with the P-nozzle are slightly reduced compared to the RS-nozzle, which can be explained by the complete lack of premixed combustion phase (Figure 4).

3.1.2. Operating Point 2

When considering an OP with higher load and engine speed (OP_2) as shown in Figure 6, in contrast to a load point with lower $BMEP$, the UCV with OME is energized earlier and longer than with diesel. Additional values of important variables for OP_2 can be taken from Table 5. The TOE must be selected significantly longer to compensate for the lower LHV of OME due to the additional fuel mass required. A much higher p_{inj} and the required higher fuel mass with OME result in a significantly larger $FMEP$ at this OP for all COCs (Table 5), and the injection system friction losses for the P-nozzle are larger than for the RS-nozzle. These losses can no longer be compensated by a higher oil temperature and thus lower engine oil viscosity at this OP. The decrease in $FMEP$ when shifting the COC toward late timings for all nozzles and fuels could be explained due to the reduced gas force on the piston rings due to the lower maximum cylinder pressure, which decreases the contact force between the piston rings and cylinder wall [78]. In addition, reduced forces

occur in the journal bearings of the crankshaft and connecting rod bearings, resulting in reduced friction losses [78]. A detailed loss distribution calculation is only possible with a very high measurement effort and is not possible in the course of this work.
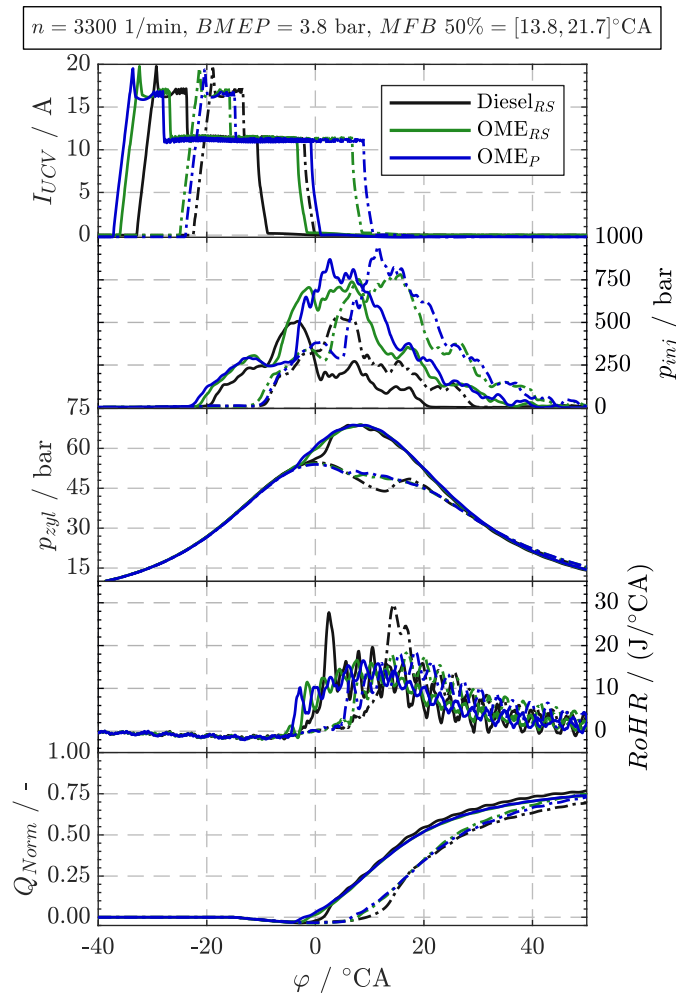

Figure 6. Drive current of high−pressure pump solenoid valve, pressure in injection line, cylinder pressure, rate of heat release and normalized released heat as a function of crank angle at two different *MFB* 50% timings for OP$_2$ and for two different nozzles in OME−operation. Solid lines *MFB* 50% = 13.8 °CA, dashed lines *MFB* 50% = 21.7 °CA.

Table 5. Additional measurement values of OP$_2$ corresponding to Figure 6.

OP$_1$	*TOE* μs		*SOE* °CA BTDC		η_i %		*FMEP* bar		*MFB* 5% °CA ATDC		*BD*$_{5-90}$ °CA		*BD*$_{50-90}$ °CA		$p_{inj, max}$ bar	
$\frac{MFB\ 50\%}{°CA\ ATDC}$	13.8	21.7	13.8	21.7	13.8	21.7	13.8	21.7	13.8	21.7	13.8	21.7	13.8	21.7	13.8	21.7
Diesel$_{RS}$	1145	1042	33.5	23.0	44	39	1.96	1.90	1.7	10.4	41.5	44.7	29.4	33.1	504	529
OME$_{RS}$	1680	1632	36.7	25.6	42	41	2.05	1.96	−0.3	8.0	42.5	40.8	28.5	27.1	739	780
OME$_P$	1879	1699	37.9	24.6	43	40	2.16	2.02	−1.0	7.0	42.4	42.2	27.6	27.7	876	950

The maximum cylinder pressure is the same for both nozzles and fuels at early COC (*MFB* 50% = 13.8 °CA), but the cylinder pressure increases with a significantly larger gradient at the start of combustion and at a later crank angle for diesel. This is due to the longer τ_{ign} and the resulting high premixed fuel fraction in diesel operation, which results in a high conversion rate during the first phase of combustion. In the case of

OME, no premixed combustion phase can be detected for both COCs and for both nozzles, which is due to the short τ_{ign} and the described greater independence of combustion from mixture-bidding processes. The conversion rate of OME is purely limited by the fuel mass flow of the nozzle and thus by the injection system. The combustion of the small injection mass during the rate-shaping phase of the RS-nozzle can also be seen here in OME operation by a slight increase in the *RoHR* curve. However, the post-spray is not discernible, which could be due to a change in the closing behavior of the RS-nozzle at long actuating durations and high injection pressures (faster closing). The conversion rate increases for OME because of the rising p_{inj} during injection and the resulting higher fuel mass flow. For the early COC, diesel combustion starts later but overtakes the total heat conversion in OME operation, resulting in a slightly shorter BD_{5-90} and higher η_i for diesel.

With the state of production injection system, it is not possible to inject the required amount of energy into the combustion chamber in a sufficiently short time at high engine speeds and loads. As a result, the BD_{5-90} with OME is extended to values similar to those with diesel, despite the significantly better ignition characteristics and faster burnout. The higher heat losses with OME because of evaporation (more mass and higher enthalpy of vaporization) and interaction of injection spray with piston surface leads to a reduced indicated efficiency with comparable burning duration. This disadvantage could only be compensated by nozzle adaptation in the form of an increased nozzle flow rate, which significantly reduces the BD_{5-90} whereby, despite higher heat losses, a significant increase in the indicated efficiency can be expected with OME.

At late COC (*MFB* 50% = 21.7 °CA), diesel shows a predominantly premixed combustion with long ignition delay, similar to OP$_1$, which leads to a steep pressure rise. Due to the low temperatures and pressures during the expansion phase, the mixture formation processes are affected in a negative way, which prolongs the BD_{5-90} for diesel. The *RoHR* of OME shows a similar course for both nozzles at the early and late COC. Due to an earlier start of injection and the shorter ignition delay, OME combustion at late COC starts closer to TDC and thus at a higher pressure and temperature level than with diesel combustion. The fuel is continuously fed to the combustion chamber, which is why diffusion-controlled combustion is observed at approximately constant pressure. Despite the constant pressure combustion, OME shows for a late COC a shorter BD_{5-90} and a slightly higher η_i than diesel. This is mainly due to faster burnout in the late expansion phase and more complete fuel conversion because of oxygen in the molecular structure.

The differences between the P- and RS-nozzle on thermodynamics are small, as the nozzles have similar maximum flow rates and the injection rates differ mainly in the opening and closing process. Due to the lower LHV of OME and longer actuation time, the influence of the opening and closing phases decreases, since the amount of energy supplied there takes up a smaller share of the total energy conversion. With increasing engine speed and load, the influence of these phases decreases. This leads to minor differences in heat release.

The trends for τ_{ign}, T_{Exh}, T_{oil} and combustion noise of OP$_2$ are similar to OP$_1$ (Figure 5a–d).

3.2. Emissions

In Figure 7, various effective emission values for OP$_1$ are shown. Due to the reduced LHV of OME, the brake-specific fuel consumption (*BSFC*) with OME increases by about 2.21 times compared to diesel operation assuming the same efficiency (Figure 7a). At late COC, fuel consumption increases for all nozzles and fuels due to reduced combustion efficiency.
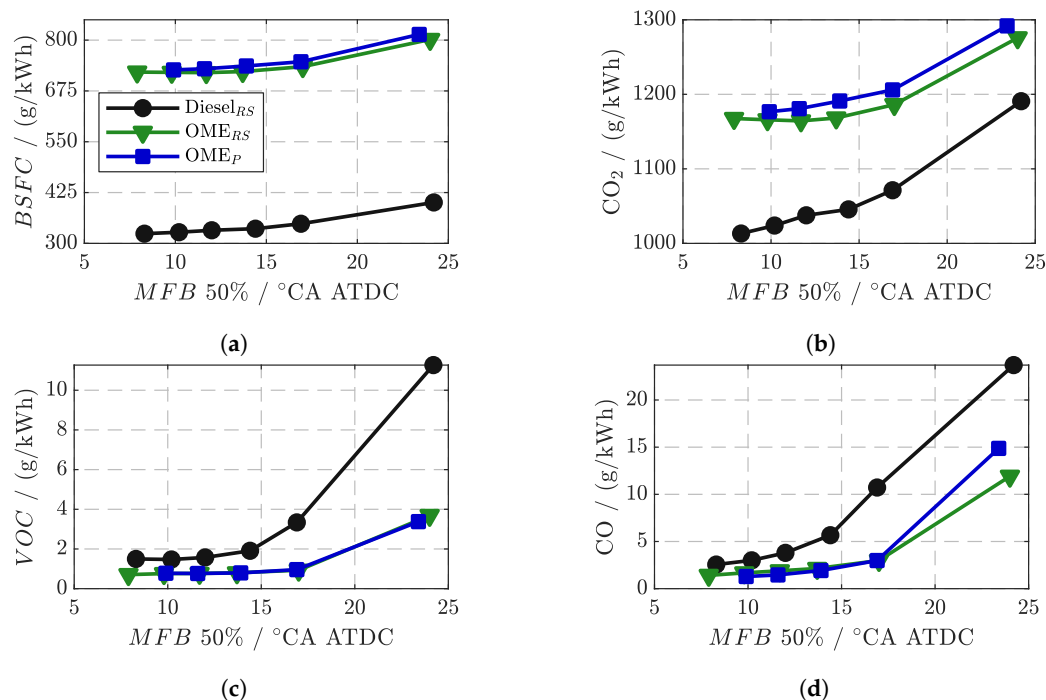
Figure 7. Brake-specific fuel consumption (**a**) and different specific effective emissions (**b**–**d**) for a variation of MFB 50% at OP_1 ($n = 2600$ 1/min, $BMEP = 2.2$ bar) for two different nozzles in OME operation.

The specific effective CO_2 emissions (Figure 7b) for OME combustion are higher than for diesel because complete combustion produces more CO_2 due to the molecular structure (see CO_2 factor in Table 1). The difference in CO_2 emissions between OME and diesel decreases at late COC because diesel combustion efficiency decreases more at late COC than with OME. In order to achieve low CO_2 emissions in a tank-to-wheel consideration with OME, the efficiency would have to be significantly increased compared to diesel operation, which only seems possible through extensive hardware adaptation or a completely new development of an engine optimized for OME. However, if the OME used is produced from renewable sources and a well-to-wheel analysis is applied, OME has a clear advantage over fossil diesel fuel in terms of the overall CO_2 balance.

Looking at the specific VOC and CO emissions in Figure 7c,d, it can be seen that emissions increase with late COC for both fuels and both nozzles. Since combustion occurs far into the expansion phase, low temperatures prevail in the combustion chamber at the end of combustion, causing the oxidation reaction to freeze, and thus, the intermediates formed can no longer be fully oxidized, resulting in increased products of incomplete combustion. In addition, mixture formation is impaired due to lower turbulence in the combustion chamber and impaired jet decay due to low backpressure and low temperatures, resulting in increased areas of rich mixture and the detection of higher VOC and CO concentrations in the exhaust gas. In addition, very late COC can result in interactions of the fuel jet with the combustion chamber wall and the engine oil thereon, resulting in increased ejection of unburned fuel and oil residues. No significant difference can be observed between the two nozzles with OME. The lower VOC and CO emissions with OME are due to the oxygen content in the molecular structure, since there are fewer areas with a local rich mixture than with diesel. In addition, the lower boiling point of OME and the significantly higher injection pressure result in improved mixture formation. Furthermore, the higher CN and the shorter combustion duration ensure that combustion is completed earlier than with diesel, which is why freezing of the oxidation reaction in the expansion phase is avoided. Overall, it can be concluded from the course of the curve that similar to the ignition delay with OME, a reduced dependency on the center of combustion and on the parameters determining the mixture formation, such as injection pressure and turbulence,

can be observed. When measuring oxygen-containing molecules (C1 structure of OME) with the FID, a response factor smaller than 1 needs to be considered [63].

The particle number measured with the SPCS and the normalized particle mass as a function of COC for OP_1 and OP_2 are shown in Figure 8. At low load and medium engine speed (Figure 8a), the PN initially increases with diesel as the COC becomes later and decreases again at very late COC positions. The same behavior is also evident in the median of the particle mobility diameter ($D_{P, \text{Median}}$) (Figure 8a, right axis). Due to the shift of combustion to the expansion phase, mixture formation is negatively affected by lower temperatures and combustion chamber pressures, which is why zones with rich mixture occur more frequently in the combustion chamber. This results in an increased formation of soot particles and promotes agglomeration into larger particles at low temperatures [79]. In addition, the oxidation reaction stops during the expansion phase due to low temperatures. The reduction in particle number at very late COC and with diesel can be explained by the high conversion rates due to a large premixing fraction (see *RoHR* Figure 4). Due to a very long ignition delay phase, a partially homogeneous mixture is formed in the combustion chamber which burns at a high conversion rate, resulting in fewer rich zones and a higher oxidation rate than the pyrolysis rate because of high temperatures [80].
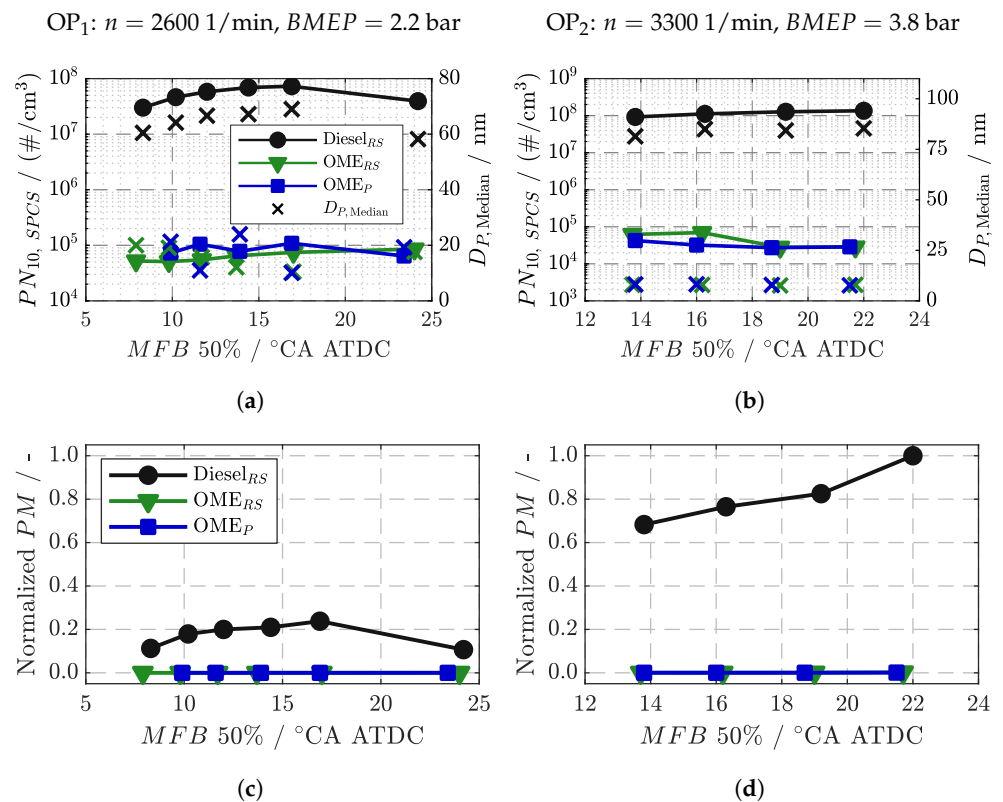

Figure 8. Measured particle number with SPCS (**a**,**b**, left axis), median of particle diameter from SMPS (**a**,**b**, right axis) and normalized particle mass from Micro Soot Sensor (**c**,**d**) at OP_1 and OP_2 for diesel and two different nozzles in OME operation.

For OP_2 and diesel, the PN and D_P also increase slightly with later COC (Figure 8b). Due to the higher engine speed and load, less time is available for mixture formation and post-oxidation of particles during the expansion phase, which is why diesel produces more PN and larger particles compared to OP_1 despite the higher temperature level and thus improved oxidation. In addition, a reduced λ at high load leads to increased soot formation due to oxygen deficiency. Better atomization because of the significantly higher maximum injection pressure at OP_2 cannot compensate for these disadvantages.

With OME, there is a reduction of about three orders of magnitude for PN_{10} at both OPs compared to diesel (Figure 8a,b). The $D_{P, \text{Median}}$ shifts from about 60–85 nm with diesel

to particles with a mobility diameter of only 10–20 nm with OME. Therefore, SPCS measurements with OME must take into account that counting efficiency decreases sharply at $D_P < 23$ nm, so dependencies of PN on the COC in this range cannot be fully resolved with SPCS. No significant differences exist between the nozzles with OME, and no dependence of PN and D_P on COC is evident.

The significant reduction of PN with OME is mainly due to the missing C-C bonds. Investigations with laminar OME flames showed that due to the missing C-C bonds in the molecular structure, no detectable typical soot precursors as with hydrocarbons (e.g., acetylene) are formed during the combustion of OME even under very rich conditions, but mainly oxygenated species such as formaldehyde and methyl formate are formed [31,32]. These precursors are largely responsible for the formation of PAHs, and the initial ring formation rate is in turn the controlling factor for soot emissions [30]. However, due to the complex conditions in the combustion chamber, formation of such soot precursors, e.g., by burning engine oil, cannot be completely prevented. With OME, however, only a few PAHs are formed, resulting in fewer particles and preventing agglomeration into larger particles. Another reason for the reduced particles is the shorter combustion time. Overall, fewer and smaller particles are formed during the main combustion phase, which is why post-oxidation is completed earlier during the expansion phase, preventing oxidation freeze-up. The soot oxidation rates during the burnout phase are also increased due to the availability of oxygen in the molecule [13]. The low residual level of particulates could also originate from metallic abrasion of the injector or engine components [20,21].

The PM emissions (Figure 8c,d) for diesel show the same trend as the PN. With OME, the measured PM concentration of the Micro Soot Sensor, using the lowest dilution level, is located within the measurement noise for both nozzles and thus at the detection limit, as also observed previously by [15,50]. Therefore, the PM emissions are reduced by more than 99% for OME compared to diesel.

Figure 9 shows the PSD for three different COCs in diesel and OME operation for OP_1 and OP_2. At both OPs, diesel predominantly produces particles with a mobility diameter >23 nm (PN_{23}) whereas in OME combustion, the peak of the PSD shifts toward the nucleation mode. The PN_{23} in the raw exhaust gas approaches the ambient level of the test cell with OME for both OPs.

At low load and engine speed (Figure 9a), with OME, there is no dependence of the PSD on the start of injection and on the injection nozzle. The PN in nucleation mode is at the same level as for diesel. The PN_{23} are reduced by several orders of magnitude with OME compared to diesel. Comparing Figures 7c and 9a, it is noticeable that the increase in VOC emissions with late COC does not occur in PSD. This indicates that the Catalytic Stripper removes all volatile components and that they are most likely solid particles. It should also be noted that the counting efficiency of the SMPS decreases for very small particles and the loss curve of the CS must be considered, so there is some uncertainty in the nucleation mode.

At higher load and engine speed (Figure 9b), with OME (both nozzles), the particles in nucleation mode increase compared to diesel, and a further increase in particle number is observed as the COC is shifted toward late timings. At higher engine speeds, less time is available for mixture formation, and the λ decreases with increasing load due to the larger injection mass, causing the PN to increase. At the same time, the temperature level increases, and therefore, the primary particle size decreases with engine load because of improved oxidation compared to OP_1 [81]. Due to the significantly increased actuation time and high injection pressure with OME at high load, it is possible for the injection jet to impinge on the piston or cylinder wall, washing off and burning engine oil. Dworschak et al. [52] also observed an increase in particle number in nucleation mode and a bimodal size distribution at unfavorable operating conditions (idle and full load) in engine tests with OME_{2-6} and also suspect a combustion of engine oil due to unfavorable operating conditions.
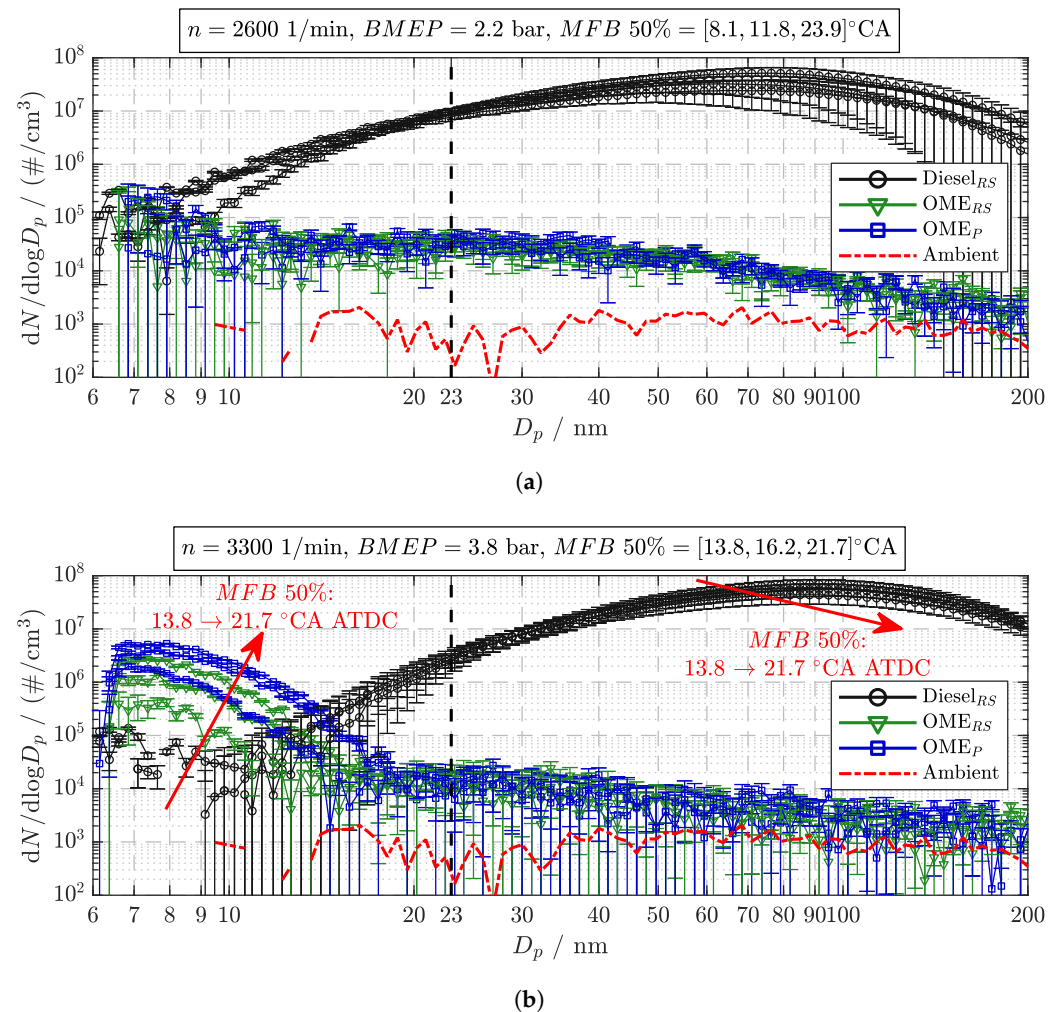
(a)

(b)

Figure 9. Particle size distribution for three different *MFB* 50% at OP$_1$ (**a**) and OP$_2$ (**b**) for diesel and two different nozzles in OME operation. Hint: Size distribution for *MFB* 50% = 8.1°CA ATDC could not be measured for P-nozzle in (**a**).

The increase in *PN* as the COC becomes later (Figure 9b) could be explained by a further deterioration of conditions in the combustion chamber. On the one hand, a further aggravation of the previously described interaction between the injection jet and the cylinder wall is to be expected due to the low backpressure, and on the other hand, a large part of the combustion takes place very late in the expansion phase, which is why the oxidation reaction stops due to low temperatures, resulting in an increased ejection of small particles. In the case of the P-nozzle, the slightly higher injection pressure and the inadequate matching of the nozzle to the combustion chamber, as well as the steeper injection rate curve, could be the cause of the slightly higher *PN* compared to the RS-nozzle.

In summary, there is a significant reduction in particle number and soot mass with OME due to the absence of C–C bonds and the particle size shifts to particles in nucleation mode, as has been widely reported [18,21,50–52]. Furthermore, the observations of [52] regarding particle formation in nucleation mode with OME under unfavorable operation conditions can be confirmed. It can be concluded that the formation of nanoparticles does not result solely from the fuel properties of OME and that special attention must be paid to the avoidance of nanoparticles in engine calibration and combustion process development.

3.3. NO$_x$ and Efficiency Potential Through Calibration

When considering the specific effective NO$_x$ emissions and varying the COC at OP$_1$ (Figure 10a top) and OP$_2$ (Figure 10b top), in OME operation, a reduction in NO$_x$

emissions of about 20–30% can be observed compared to diesel. NO_x emissions increase for all fuels and nozzles exponentially at COC closer to TDC, which is due to the formation of thermal NO because of higher cylinder pressure and associated temperature increase in the combustion chamber. The difference in NO_x emissions between both nozzles in OME operation is small because the *RoHR* (see Section 3.1, Figures 4 and 6) is nearly similar for both investigated OPs. The reason for the reduction in NO_x emissions with OME is the significantly higher injected fuel mass, whereby heat is extracted from the combustion chamber charge during evaporation and peak temperatures decrease as a result. A stoichiometric combustion of OME produces larger amounts of water and CO_2 due to its molecular composition (CO_2 and H_2O factor in Table 1), which increases the specific heat capacity of the combustion chamber charge and in turn results in lower peak temperatures and NO_x [66]. Assuming the same efficiency, all OPs with the same power output and the same aspirated air mass (naturally aspirated engine) result in a larger λ than with diesel due to a smaller ratio of AFR/LHV (Table 1) of OME [20]. The higher λ results in a significantly lower adiabatic flame temperature (AFT) for OME, and the AFT increases less with rising engine load ($\lambda \downarrow$) than for diesel, which further increases the differences in AFT at high engine loads [20]. This leads to reduced NO_x emissions with OME, but effects of reaction kinetics, energy release rate, local peak temperatures, etc. on NO_x formation are not considered here. Another reason for the lower NO_x emissions with OME is the lower maximum energy conversion rate, since no premixed combustion phase occurs as in diesel operation due to the short ignition delay, and the maximum amount of energy converted is limited by the unchanged nozzle diameter (Figures 4 and 6). Previous studies showed that the NO_x reduction potential without EGR increases with chain length of OME_n and therefore depends on the fuel composition [20,33,66,82].
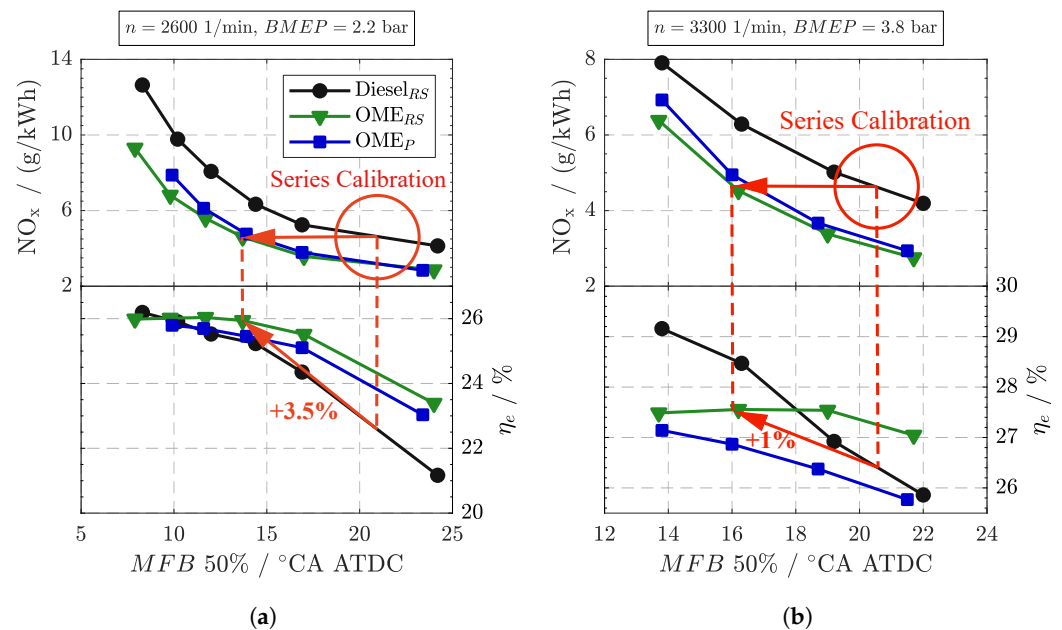

Figure 10. Specific effective NO_x-emissions and effective efficiency for a variation of *MFB* 50% at OP_1 (**a**) and OP_2 (**b**) for diesel and two different nozzles in OME operation.

Since the series engine does not have the option of controlled EGR for NO_x reduction and an SCR exhaust gas aftertreatment system is very cost-intensive, the COC of the series calibration is set to more than 20 °CA ATDC over a large part of the operating range in order to keep NO_x emissions at a low level and to meet government regulations. The strong reduction of NO_x emissions in OME operation thus opens up a new degree of freedom in the calibration of the series engine, whereby the COC can be shifted significantly toward TDC for the same NO_x emissions (Figure 10a top). This can increase the effective efficiency of the engine by about 3.5% points in the medium load and speed range without hardware

adaptation (RS-nozzle), while complying with NO_x limits (Figure 10a bottom). At high loads and speeds (Figure 10b bottom), a reduced potential ($\approx$1 percent point) is shown, since the series injection system is limited in flow. The required amount of energy cannot be injected into the combustion chamber in a sufficiently short time, resulting in longer combustion durations, and thus, heat and efficiency losses occur (Section 3.1, Figure 6). In addition, at high loads and engine speeds, the friction losses of the injection system increase due to the extra mass and high injection pressures. With the P-nozzle, a slight efficiency disadvantage is evident at both OPs, which can be attributed to inadequate matching of the nozzle to the HPP and maybe different spray pattern and piston or wall impingement with the spray (higher p_{inj}). The effect of the different injection rate curve during the opening phase plays a minor role on NO_x formation in OME operation due to the short ignition delay, and it is mainly through diffusion controlled combustion.

4. Conclusions

Investigations were carried out on a close-to-production single-cylinder diesel engine with a pump–line–nozzle injection system using an OME_{3-6} mixture and diesel as a reference. Variations of the center of combustion were carried out at two different operating points, and two nozzles with different injection rate curves were measured for OME.

The thermodynamic analysis of the OPs showed that with OME, despite a longer *TOE*, significantly shorter burn durations occur, which can be attributed to higher oxidation rates due to the oxygen bond in the molecule, the low soot formation and thus faster completion of post-oxidation in the burnout phase, and the high cetane number. The shorter burn duration with OME results in higher indicated efficiency, especially at low loads, although greater heat losses occur with OME ($\uparrow T_{Oil}$) compared to diesel. These are due to the extended *TOE* and the interaction of the injection jet and flame with the piston surface. The higher fuel mass to be evaporated and a higher specific heat capacity of the combustion chamber charge (more CO_2 and H_2O) lead to higher heat losses.

In a PLN injection system, the injection pressure and thus the mass flow increase strongly due to the extended *TOE*, which means that the LHV disadvantage can be partially compensated without nozzle adjustment.

The differences between the P- and RS-nozzle in terms of emissions and efficiency are small, as the nozzles have similar maximum flow rates and the injection rates differ mainly in the opening and closing process. Due to the lower LHV, shorter ignition delay and longer actuation time with OME, the influence of these phases decreases, since the amount of energy supplied there takes up a smaller share of the total energy conversion.

The *FMEP* increases with rising load for OME due to the additional effort required for fuel delivery and the higher injection pressure. At certain OPs, a higher oil temperature due to the higher heat losses could lead to reduced friction in the engine and partially compensate for this disadvantage. The piston is probably subjected to higher thermal loads in OME operation without adjustment of the nozzle flow.

For OME, a significantly shorter ignition delay and a lower dependence of the ignition delay on the *SOI* and thus on the flow and temperature conditions in the combustion chamber were observed than with diesel (lower boiling point, oxygen in the molecule reduces influence of air entrainment). The shorter ignition delay and lower LHV of OME reduces the premixed fraction, which decreases the maximum conversion rate and significantly reduces noise emissions.

Significantly reduced *VOC*, CO, *PM* and *PN* emissions indicate more complete combustion of OME. Particle number and soot mass decrease significantly with OME due to the absence of C-C bonds and higher oxidation rates because of oxygen in the molecular structure. The median of particle size shifts with OME to particles in the nucleation mode (<23 nm). Particle formation in the nucleation mode with OME was observed under unfavorable operating conditions, which could be caused by the combustion of engine oil, as a result of impingement of the injection jet on the piston crown or cylinder wall due to long injection durations and high injection pressures.

The reduction of NO_x emissions opens up new degrees of freedom in the calibration of the series engine, allowing an increase in efficiency while complying with current NO_x regulations through software adaptation. At high loads, the potential for efficiency improvements decreases due to the limited nozzle flow.

The results show that fuel switching to OME, especially for simple engines with rudimentary fuel injection technology and no means of NO_x reduction (no EGR or SCR), opens up enormous potential for increasing efficiency while reducing all regulated pollutants (NO_x, *PN*, *PM*, CO, and *VOC*).

Abbreviations

The following abbreviations are used in this manuscript:

AFR	Air–Fuel Ratio
AFT	Adiabatic Flame Temperature
ATDC	After Top Dead Center
BD	Burning Duration
BMEP	Break Mean Effective Pressure
BSFC	Break Specific Fuel Consumption
BTDC	Before Top Dead Center
CA	Crank Angle
CN	Cetane Number
CO	Carbon Monoxide
CO_2	Carbon Dioxide
COC	Center of Combustion
CPC	Condensation Particle Counter
CS	Catalytic Stripper
DMA	Differential Mobility Analyzer
D_P	Particle diameter
ECU	Engine Control Unit
EGR	Exhaust Gas Recirculation
EPDM	Propylene Diene Rubber
η_i	Indicated Efficiency
η_e	Effective Efficiency
FA	Formaldehyde
FAME	Fatty Acid Methyl Ethers
FID	Flame Ionization Detector

FKM	Flourine Rubber
FFKM	Perfluoroelastomers
FMEP	Friction Mean Effective Pressure
HFRR	High-Frequency Reciprocating Rig
HPP	High-Pressure Pump
IMEP	Indicated Mean Effective Pressure
LHV	Lower Heating Value
MSS	Micro Soot Sensor
MeOH	Methanol
n	Engine Speed
NO_x	Nitrogen Oxides
τ_{ign}	Ignition Delay Time
MFB	Mass Fuel Burned
OME	Oxymethylene Ether
OP	Operating Point
P	Proportional Nozzle
PLN	Pump–Line–Nozzle
PM	Particulate Matter
PN	Particle Number
PN_{10}	Particle Number, diameter $\geq$ 10 nm
PN_{23}	Particle Number, diameter $\geq$ 23 nm
PSD	Particle Size Distribution
PTFE	Polytetrafluoroethylene
PtL	Power to Liquid
RoHR	Rate of Heat Release
RS	Rate Shaping
SMPS	Scanning Mobility Particle Sizer
SOE	Start of Energizing
SOI	Start of Injection
SPCS	Solid Particle Counting System
TDC	Top Dead Center
TOE	Time of Energizing
UCV	Unit Control Valve of High Pressure Pump
VOC	Volatile Organic Compounds

References

1. Masson-Delmotte, V.; Zhai, P.; Pörtner, H.-O.; Roberts, D.; Skea, J.; Shukla ,P.R.; Pirani, A.; Moufouma-Okia, W.; Péan, C.; Pidcock, R.; et al. IPCC, 2018: Global Warming of 1.5 °C. An IPCC Special Report on the impacts of global warming of 1.5 °C above pre-industrial levels and related global greenhouse gas emission pathways, in the context of strengthening the global response to the threat of climate change, sustainable development, and efforts to eradicate poverty. Cambridge University Press, Cambridge, UK and New York, NY, USA, 616 pp. https://doi.org/10.1017/9781009157940.
2. Omari, A.; Heuser, B.; Wiartalla, A.; Bergmann, D. Stromgenerierte Kraftstoffe für mobile Maschinen. *ATZ Offhighway* **2018**, *11*, 42–47. https://doi.org/10.1007/s35746-018-0016-0.
3. Schlögl, R. Erneuerbare Energien in der Mobilität: Das Potential synthetischer kraftstoffe auf der Basis von CO2. In *Proceedings of the 39 Internationales Wiener Motorensymposium*; Geringer, B., Lenz, H.P., Eds.; Fortschritt-Berichte VDI. Reihe 12, Verkehrstechnik, Fahrzeugtechnik; VDI Verlag GmbH: Düsseldorf, Germany, 2018; pp. 191–201.
4. Backhaus, R. Alternative Kraftstoffe CO2-neutral in die Zukunft. *MTZ-Mot. Z.* **2017**, *78*, 9–14.
5. Burger, J. *A Novel Process for the Production of Diesel Fuel Additives by Hierarchical Design: Zugl*; Scientific Report Series/Laboratory of Engineering Thermodynamics; Technical University of Kaiserslautern: Kaiserslautern, Germany, 2012; Volume 3.
6. Hackbarth, K.; Haltenort, P.; Arnold, U.; Sauer, J. Recent Progress in the Production, Application and Evaluation of Oxymethylene Ethers. *Chem. Ing. Tech.* **2018**, *90*, 1520–1528. https://doi.org/10.1002/cite.201800068.
7. Baranowski, C.J.; Bahmanpour, A.M.; Kröcher, O. Catalytic synthesis of polyoxymethylene dimethyl ethers (OME): A review. *Appl. Catal. B Environ.* **2017**, *217*, 407–420. https://doi.org/10.1016/j.apcatb.2017.06.007.
8. Schmitz, N.; Burger, J.; Ströfer, E.; Hasse, H. From methanol to the oxygenated diesel fuel poly(oxymethylene) dimethyl ether: An assessment of the production costs. *Fuel* **2016**, *185*, 67–72. https://doi.org/10.1016/j.fuel.2016.07.085.
9. Oestreich, D. Prozessentwicklung zur Gewinnung von Oxymethylenethern (OME) aus Methanol und Formaldehyd. Ph.D. Thesis, Karlsruher Institut für Technologie, Karlsruhe, Germany, 2017. https://doi.org/10.5445/KSP/1000069417.

10. Oestreich, D.; Lautenschütz, L.; Arnold, U.; Sauer, J. Production of oxymethylene dimethyl ether (OME)-hydrocarbon fuel blends in a one-step synthesis/extraction procedure. *Fuel* **2018**, *214*, 39–44. https://doi.org/10.1016/j.fuel.2017.10.116.

11. Held, M.; Tönges, Y.; Pélerin, D.; Härtl, M.; Wachtmeister, G.; Burger, J. On the energetic efficiency of producing polyoxymethylene dimethyl ethers from CO 2 using electrical energy. *Energy Environ. Sci.* **2019**, *12*, 1019–1034. https://doi.org/10.1039/C8EE02849D.

12. Wilharm, T.; Stein, H.; Bogatykh, I. Roadmap to an OME specification. In *Internationaler Motorenkongress 2020*; Liebl, J., Beidl, C., Maus, W., Eds.; Springer Fachmedien Wiesbaden: Wiesbaden, Germany, 2020; pp. 205–211. https://doi.org/10.1007/978-3-658-30500-0_13.

13. Pellegrini, L.; Marchionna, M.; Patrini, R.; Beatrice, C.; Del Giacomo, N.; Guido, C. Combustion Behaviour and Emission Performance of Neat and Blended Polyoxymethylene Dimethyl Ethers in a Light-Duty Diesel Engine. *SAE Tech. Pap.* **2012**. https://doi.org/10.4271/2012-01-1053.

14. Härtl, M. Emissionsreduktion bei Dieselmotoren durch den Einsatz sauerstoffhaltiger Kraftstoffe. Ph.D. Thesis, Technische Universität München, München, Germany, 2015.

15. Münz, M.; Töpfer, D.; Mokros, A.; Beidl, C. Oxygenate fuel in a Diesel engine—Is a CI engine capable of lambda 1? In *Internationaler Motorenkongress 2017*; Liebl, J., Beidl, C., Eds.; Springer Fachmedien Wiesbaden: Wiesbaden, Germany, 2017; pp. 457–472. https://doi.org/10.1007/978-3-658-17109-4_29.

16. Pélerin, D.; Gaukel, K.; Härtl, M.; Wachtmeister, G. Recent results of the sootless Diesel fuel oxymethylene ether. In *Internationaler Motorenkongress 2017*; Liebl, J., Beidl, C., Eds.; Springer Fachmedien Wiesbaden: Wiesbaden, Germany, 2017; pp. 439–456. https://doi.org/10.1007/978-3-658-17109-4_28.

17. Härtl, M.; Pélerin, D.; Gaukel, K.; Dworschak, P.; Wachtmeister, G. OME als Reinstoff: Emissionsreduktion bei Dieselmotoren durch sauerstoffhaltige synthetische Kraftstoffe. In *Zukünftige Kraftstoffe*; Maus, W., Ed.; Springer: Berlin/Heidelberg, Germany, 2019; Volume 89, pp. 799–813. https://doi.org/10.1007/978-3-662-58006-6_31.

18. Omari, A.; Heuser, B.; Pischinger, S.; Rüdinger, C. Potential of long-chain oxymethylene ether and oxymethylene ether-diesel blends for ultra-low emission engines. *Appl. Energy* **2019**, *239*, 1242–1249. https://doi.org/10.1016/j.apenergy.2019.02.035.

19. Pélerin, D.; Gaukel, K.; Härtl, M.; Jacob, E.; Wachtmeister, G. Potentials to simplify the engine system using the alternative diesel fuels oxymethylene ether OME1 and OME3−6 on a heavy-duty engine. *Fuel* **2020**, *259*, 116231. https://doi.org/10.1016/j.fuel.2019.116231.

20. Pélerin, D. Potentiale der Synthetischen Kraftstoffe Oxymethylenether und Dimethylether zur Realisierung Klimaneutraler, Schadstoffarmer Sowie Vereinfachter Dieselmotoren. Ph.D. Thesis, Technische Universität München, München, Germany, 2021.

21. Barro, C.; Parravicini, M.; Boulouchos, K.; Liati, A. Neat polyoxymethylene dimethyl ether in a diesel engine; Part 2: Exhaust emission analysis. *Fuel* **2018**, *234*, 1414–1421. https://doi.org/10.1016/j.fuel.2018.07.108.

22. Gaukel, K.; Pélerin, D.; Härtl, M.; Wachtmeister, G.; Burger, J.; Maus, W.; Jacob, E. Der Kraftstoff OME2: Ein Beispiel für den Weg zu emissionsneutralen Fahrzeugen mit Verbrennungsmotor. In *Proceedings of the 37 Internationales Wiener Motorensymposium*; Lenz, H.P., Ed.; Fortschritt-Berichte VDI. Reihe 12, Verkehrstechnik, Fahrzeugtechnik; VDI Verlag GmbH: Düsseldorf, Germany, 2016; pp. 193–223.

23. García, A.; Gil, A.; Monsalve-Serrano, J.; Lago Sari, R. OMEx-diesel blends as high reactivity fuel for ultra-low NOx and soot emissions in the dual-mode dual-fuel combustion strategy. *Fuel* **2020**, *275*, 117898. https://doi.org/10.1016/j.fuel.2020.117898.

24. Damyanov, A.; Hofmann, P.; Drack, J.; Pichler, T.; Schwaiger, N.; Siebenhofer, M. Operation of a Diesel Engine with Biogenous Oxymethylene Ethers. In Proceedings of the 26. Aachener Kolloquium Fahrzeug- und Motorentechnik, Aachen, Germany, 9–11 October 2017.

25. Parravicini, M.; Barro, C.; Boulouchos, K. Compensation for the differences in LHV of diesel-OME blends by using injector nozzles with different number of holes: Emissions and combustion. *Fuel* **2020**, *259*, 116166. https://doi.org/10.1016/j.fuel.2019.116166.

26. Damyanov, A. Diesel-OME-Blends. In *Zukünftige Kraftstoffe*; Maus, W., Ed.; Springer: Berlin/Heidelberg, Germany, 2019; Volume 52, pp. 918–928. https://doi.org/10.1007/978-3-662-58006-6_39.

27. Omari, A.; Heuser, B.; Pischinger, S. Potential of oxymethylenether-diesel blends for ultra-low emission engines. *Fuel* **2017**, *209*, 232–237. https://doi.org/10.1016/j.fuel.2017.07.107.

28. Popp, T.; Lechner, R.; Becker, M.; Hebauer, M.; O'Connell, N.; Brautsch, M. Potentials of OME/diesel blends for station-ary power production – Improving emission characteristics of a diesel CHP unit. *Appl. Therm. Eng.* **2019**, *153*, 483–492. https://doi.org/10.1016/j.applthermaleng.2019.03.015.

29. Preuß, J.; Munch, K.; Denbratt, I. Performance and emissions of renewable blends with OME3-5 and HVO in heavy duty and light duty compression ignition engines. *Fuel* **2021**, *303*, 121275. https://doi.org/10.1016/j.fuel.2021.121275.

30. Glassman, I. Soot formation in combustion processes. *22 Symp. Int. Combust. Combust. Inst.* **1988**, *22*, 295–311. https://doi.org/10.1016/S0082-0784(89)80036-0.

31. Gaiser, N.; Bierkandt, T.; Oßwald, P.; Zinsmeister, J.; Kathrotia, T.; Shaqiri, S.; Hemberger, P.; Kasper, T.; Aigner, M.; Köhler, M. Oxidation of oxymethylene ether (OME0−5): An experimental systematic study by mass spectrometry and photoelectron photoion coincidence spectroscopy. *Fuel* **2022**, *313*, 122650. https://doi.org/10.1016/j.fuel.2021.122650.

32. Gaiser, N.; Zhang, H.; Bierkandt, T.; Schmitt, S.; Zinsmeister, J.; Kathrotia, T.; Hemberger, P.; Shaqiri, S.; Kasper, T.; Aigner, M.; et al. Investigation of the combustion chemistry in laminar, low-pressure oxymethylene ether flames (OME0–4). *Combust. Flame* **2022**, *243*, 112060. https://doi.org/10.1016/j.combustflame.2022.112060.

33. Eckart, S.; Cai, L.; Fritsche, C.; vom Lehn, F.; Pitsch, H.; Krause, H. Laminar burning velocities, CO, and NOx emissions of premixed polyoxymethylene dimethyl ether flames. *Fuel* **2021**, *293*, 120321. https://doi.org/10.1016/j.fuel.2021.120321.

34. Schmitz, R.; Russo, C.; Ferraro, F.; Apicella, B.; Hasse, C.; Sirignano, M. Effect of oxymethylene ether-2-3-4 (OME2-4) on soot particle formation and chemical features. *Fuel* **2022**, *324*, 124617. https://doi.org/10.1016/j.fuel.2022.124617.

35. Sun, W.; Wang, G.; Li, S.; Zhang, R.; Yang, B.; Yang, J.; Li, Y.; Westbrook, C.K.; Law, C.K. Speciation and the laminar burning velocities of poly(oxymethylene) dimethyl ether 3 (POMDME3) flames: An experimental and modeling study. *Proc. Combust. Inst.* **2017**, *36*, 1269–1278. https://doi.org/10.1016/j.proci.2016.05.058.

36. Tan, Y.R.; Salamanca, M.; Pascazio, L.; Akroyd, J.; Kraft, M. The effect of poly(oxymethylene) dimethyl ethers (PODE3) on soot formation in ethylene/PODE3 laminar coflow diffusion flames. *Fuel* **2021**, *283*, 118769. https://doi.org/10.1016/j.fuel.2020.118769.

37. Li, R.; Herreros, J.M.; Tsolakis, A.; Yang, W. Chemical kinetic study on ignition and flame characteristic of polyoxymethylene dimethyl ether 3 (PODE3). *Fuel* **2020**, *279*. https://doi.org/10.1016/j.fuel.2020.118423.

38. Liu, Y.; Cheng, X.; Ya, Y.; Wang, B.; Zhang, P.; Zhang, K.; Xu, Y. Impact of PODE3 on soot oxidation reactivity at different stages in n-heptane/toluene diffusion flames. *Fuel* **2023**, *331*, 125672. https://doi.org/10.1016/j.fuel.2022.125672.

39. Cai, L.; Jacobs, S.; Langer, R.; vom Lehn, F.; Heufer, K.A.; Pitsch, H. Auto-ignition of oxymethylene ethers (OMEn, n = 2–4) as promising synthetic e-fuels from renewable electricity: Shock tube experiments and automatic mechanism generation. *Fuel* **2020**, *264*, 116711. https://doi.org/10.1016/j.fuel.2019.116711.

40. Drost, S.; Schießl, R.; Werler, M.; Sommerer, J.; Maas, U. Ignition delay times of polyoxymethylene dimethyl ether fuels (OME2 and OME3) and air: Measurements in a rapid compression machine. *Fuel* **2019**, *258*, 116070. https://doi.org/10.1016/j.fuel.2019.116070.

41. He, T.; Wang, Z.; You, X.; Liu, H.; Wang, Y.; Li, X.; He, X. A chemical kinetic mechanism for the low- and intermediate-temperature combustion of Polyoxymethylene Dimethyl Ether 3 (PODE3). *Fuel* **2018**, *212*, 223–235. https://doi.org/10.1016/j.fuel.2017.09.080.

42. Zhao, Y.; Li, N.; Xie, Y.; Cheng, Y.; Wang, X. Study on chemical kinetic mechanisms of Polyoxymethylene Dimethyl Ethers (PODE n). *IOP Conf. Ser. Mater. Sci. Eng.* **2020**, *768*, 022056. https://doi.org/10.1088/1757-899X/768/2/022056.

43. Pastor, J.V.; García, A.; Micó, C.; Lewiski, F. An optical investigation of Fischer-Tropsch diesel and Oxymethylene dimethyl ether impact on combustion process for CI engines. *Appl. Energy* **2020**, *260*, 114238. https://doi.org/10.1016/j.apenergy.2019.114238.

44. Pastor, J.V.; García, A.; Micó, C.; Lewiski, F. Simultaneous high-speed spectroscopy and 2-color pyrometry analysis in an optical compression ignition engine fueled with OMEX-diesel blends. *Combust. Flame* **2021**, *230*, 111437. https://doi.org/10.1016/j.combustflame.2021.111437.

45. Pastor, J.V.; Garcia-Oliver, J.M.; Micó, C.; Tejada, F.J. Comparison of the Diffusive Flame Structure for Dodecane and OME X Fuels for Conditions of Spray A of the ECN. *SAE Int. J. Adv. Curr. Pract. Mobil.* **2021**, *3*, 402–411. https://doi.org/10.4271/2020-01-2120.

46. Pastor, J.V.; García-Oliver, J.M.; Micó, C.; García-Carrero, A.A. An experimental study with renewable fuels using ECN Spray A and D nozzles. *Int. J. Engine Res.* **2021**, *23*, 1748–1759. https://doi.org/10.1177/14680874211031200.

47. Pastor, J.V.; García-Oliver, J.M.; Micó, C.; García-Carrero, A.A.; Gómez, A. Experimental Study of the Effect of Hydrotreated Vegetable Oil and Oxymethylene Ethers on Main Spray and Combustion Characteristics under Engine Combustion Network Spray A Conditions. *Appl. Sci.* **2020**, *10*, 5460. https://doi.org/10.3390/app10165460.

48. Ma, Y.; Cui, L.; Ma, X.; Wang, J. Optical study on spray combustion characteristics of PODE/diesel blends in different ambient conditions. *Fuel* **2020**, *272*, 117691. https://doi.org/10.1016/j.fuel.2020.117691.

49. Iannuzzi, S.E.; Barro, C.; Boulouchos, K.; Burger, J. Combustion behavior and soot formation/oxidation of oxygenated fuels in a cylindrical constant volume chamber. *Fuel* **2016**, *167*, 49–59. https://doi.org/10.1016/j.fuel.2015.11.060.

50. Münz, M.; Mokros, A.; Beidl, C. OME in the Diesel engine–A concept for CO2 neutrality and lowest pollutant emissions. In *Internationaler Motorenkongress 2018*; Liebl, J., Beidl, C., Maus, W., Motorenkongress, I., Eds.; Springer Vieweg: Wiesbaden, Germany, 2018; pp. 445–458. https://doi.org/10.1007/978-3-658-21015-1_28.

51. Richter, G.; Zellbeck, H. OME als Kraftstoffersatz im Pkw-Dieselmotor. *MTZ-Mot. Z.* **2017**, *78*, 66–73. https://doi.org/10.1007/s35146-017-0131-y.

52. Dworschak, P.; Berger, V.; Härtl, M.; Wachtmeister, G. Particle Size Distribution Measurements of Neat and Water-Emulsified Oxymethylene Ethers in a Heavy-Duty Diesel Engine. *SAE Int. J. Fuels Lubr.* **2020**, *13*, 187–204. https://doi.org/10.4271/04-13-02-0012.

53. *DIN EN 590:2022*; Kraftstoffe- Dieselkraftstoff- Anforderungen und Prüfverfahren, Deutsche Fassung EN 590:2022-05, Deutsches Institut für Normung e.V., Beuth Verlag GmbH, Berlin, 2022. https://dx.doi.org/10.31030/3337114.

54. Jacob, E.; Maus, W. Oxymethylenether als potenziell CO2-neutraler Kraftstoff für saubere Dieselmotoren Teil 2: Erfüllung des Nachhaltigkeitsanspruchs: Teil 2: Erfüllung des Nachhaltigkeitsanspruchs. *MTZ-Mot. Z.* **2017**, *78*, 54–61. https://doi.org/10.1007/s35146-017-0017-z.

55. Härtl, M.; Seidenspinner, P.; Jacob, E.; Wachtmeister, G. Oxygenate screening on a heavy-duty diesel engine and emission characteristics of highly oxygenated oxymethylene ether fuel OME1. *Fuel* **2015**, *153*, 328–335. https://doi.org/10.1016/j.fuel.2015.03.012.

56. Uchida, T.; Kurita, Y.; Kubo, M. The dipole moments and the structure of polyoxymethylene dimethyl ethers. *J. Polym. Sci.* **1956**, *19*, 365–372. https://doi.org/10.1002/pol.1956.120199215.

57. Boehman, A.L.; Morris, D.; Szybist, J.; Esen, E. The Impact of the Bulk Modulus of Diesel Fuels on Fuel Injection Timing. *Energy Fuels* **2004**, *18*, 1877–1882. https://doi.org/10.1021/ef049880j.

58. Tat, M.E.; Gerpen, J.H.V. *Measurement of Biodiesel Speed of Sound and Its Impact on Injection Timing: Final Report: Report 4 in a series of 6: Technical Report No. NREL/SR-510-31462*; National Renewable Energy Lab.: Golden, CO, USA, 2003.

59. Schwanzer, P.; Rabl, H.P.; Loders, S.; Seifert, P.; Himmelstoß, S.; Gaderer, M. Difference in the Tailpipe Particle Number by Consideration of Sub-23-nm Particles for Different Injection Settings of a GDI Engine. *Emiss. Control Sci. Technol.* **2019**, *5*, 7–22. https://doi.org/10.1007/s40825-019-0114-1.

60. Kittelson, D.B.; Johnson, J.H. Variability in Particle Emission Measurements in the Heavy Duty Transient Test. *SAE Tech. Pap.* **1991**, 1378–1403. https://doi.org/10.4271/910738.

61. Catalytic Instruments. *Losses in the Catalytic Stripper: Application Note CI-0009*; Catalytic Instruments GmbH & Co.KG, Rosenheim, 2020.

62. Giechaskiel, B.; Martini, G. Engine Exhaust Solid Sub-23 nm Particles: II. Feasibility Study for Particle Number Measurement Systems. *SAE Int. J. Fuels Lubr.* **2014**, *7*, 935–949. https://doi.org/10.4271/2014-01-2832.

63. Huang, Y.; Ou, Q.; Yu, W. Characteristics of flame ionization detection for the quantitative analysis of complex organic mixtures. *Anal. Chem.* **1990**, *62*, 2063–2064. https://doi.org/10.1021/ac00217a033.

64. Brettschneider, J. Berechnung des Luftverhätnisses Lambda von Luft-Kraftstoff-Gemischen und des Einflusses von Messfehlern auf Lambda. In *Bosch Technische Berichte 6*; Robert Bosch: Stuttgart, Germany, 1979; pp. 177–186.

65. Strunk, R.D. The Dynamics of Pump-Line-Nozzle Fuel Injection Systems. *SAE Tech. Pap.* **1991**. https://doi.org/10.4271/911818.

66. Dworschak, P.; Berger, V.; Härtl, M.; Wachtmeister, G. Neat Oxymethylene Ethers: Combustion Performance and Emissions of OME 2, OME 3, OME 4 and OME 5 in a Single-Cylinder Diesel Engine. *SAE Tech. Pap.* **2020**. https://doi.org/10.4271/2020-01-0805.

67. Huang, Z.H.; Ren, Y.; Jiang, D.M.; Liu, L.X.; Zeng, K.; Liu, B.; Wang, X.B. Combustion and emission characteristics of a compression ignition engine fuelled with Diesel–dimethoxy methane blends. *Energy Convers. Manag.* **2006**, *47*, 1402–1415. https://doi.org/10.1016/j.enconman.2005.08.020.

68. Ren, Y.; Huang, Z.; Miao, H.; Di, Y.; Jiang, D.; Zeng, K.; Liu, B.; Wang, X. Combustion and emissions of a DI diesel engine fuelled with diesel-oxygenate blends. *Fuel* **2008**, *87*, 2691–2697. https://doi.org/10.1016/j.fuel.2008.02.017.

69. Shimamoto, Y.; Akiyama, K. A Study of Squish in Open Combustion Chambers of a Diesel Engine. *Bull. JSME* **1970**, *13*, 1096–1103. https://doi.org/10.1299/jsme1958.13.1096.

70. Barro, C.; Parravicini, M.; Boulouchos, K. Neat polyoxymethylene dimethyl ether in a diesel engine: Part 1: Detailed combustion analysis. *Fuel* **2019**, *256*, 115892. https://doi.org/10.1016/j.fuel.2019.115892.

71. Dageförde, T.; Gröger, K.; Kawaharada, N.; Dinkelacker, F. Velocity Field Measurements with High Speed Structural Image Velocimetry in the Primary Atomization Region of Future Diesel Fuels. *SAE Int. J. Adv. Curr. Pract. Mobil.* **2021**, *3*, 378–386. https://doi.org/10.4271/2020-01-2112.

72. Röll, A.; Luo, F.; O'Connell, N.; Lechner, R.; Wang, C.; Brautsch, M. Hydraulic stability of micro injections using a two-layered 8-hole solenoid injector with PODE. *Fuel* **2021**, *297*, 120748. https://doi.org/10.1016/j.fuel.2021.120748.

73. Pöllmann, S.; Härtl, M.; Wachtmeister, G. Injection Process of the Synthetic Fuel Oxymethylene Ether: Optical Analysis in a Heavy-Duty Engine. *SAE Tech. Pap.* **2020**. https://doi.org/10.4271/2020-01-2144.

74. Weingartz, C.J.; Anderson, C.L.; Miers, S.A. Determination of Heat Transfer Augmentation Due to Fuel Spray Impingement in a High-Speed Diesel Engine. *SAE Tech. Pap.* **2009**. https://doi.org/10.4271/2009-01-0843.

75. Woschni, G.; Huber, K. The Influence of Soot Deposits on Combustion Chamber Walls on Heat Losses in Diesel Engines. *SAE Tech. Pap.* **1991**. https://doi.org/10.4271/910297.

76. Overbye, V.D.; Bennethum, J.E.; Uyehara, O.A.; Myers, P.S. Unsteady Heat Transfer in Engines. *SAE Tech. Pap.* **1961**, 34. https://doi.org/10.4271/610041.

77. Borman, G.; Nishiwaki, K. Internal-combustion engine heat transfer. *Prog. Energy Combust. Sci.* **1987**, *13*, 1–46. https://doi.org/10.1016/0360-1285(87)90005-0.

78. Kouremenos, D.A.; Rakopoulos, C.D.; Hountalas, D.T.; Zannis, T.K. Development of a Detailed Friction Model to Predict Mechanical Losses at Elevated Maximum Combustion Pressures. *SAE Tech. Pap.* **2001**. https://doi.org/10.4271/2001-01-0333.

79. Lee, K.O.; Cole, R.; Sekar, R.; Choi, M.Y.; Kang, J.S.; Bae, C.S.; Shin, H.D. Morphological investigation of the microstructure, dimensions, and fractal geometry of diesel particulates. *Proc. Combust. Inst.* **2002**, *29*, 647–653. https://doi.org/10.1016/S1540-7489(02)80083-9.

80. Tree, D.R.; Svensson, K.I. Soot processes in compression ignition engines. *Prog. Energy Combust. Sci.* **2007**, *33*, 272–309. https://doi.org/10.1016/j.pecs.2006.03.002.

81. Zhu, J.; Lee, K.O.; Yozgatligil, A.; Choi, M.Y. Effects of engine operating conditions on morphology, microstructure, and fractal geometry of light-duty diesel engine particulates. *Proc. Combust. Inst.* **2005**, *30*, 2781–2789. https://doi.org/10.1016/j.proci.2004.08.232.

82. Dworschak, P.; Berger, V.; Härtl, M.; Wachtmeister, G. Oxymethylene Ethers: Evaluating the Optimum Fuel Composition from an Engine Standpoint with Respect to Emissions and Combustion Performance. *SAE Int. J. Fuels Lubr.* **2022**, *15*, 171–179. https://doi.org/10.4271/04-15-02-0008.